Estimation of Rotor Blade Loading Distribution from Slipstream Velocity Measurements

Goyal, Jatinder; Sinnige, Tomas; Avallone, Francesco; Ferreira, Carlos

DOI
10.2514/1.J064736

Publication date
2025

Document Version
Final published version

Published in
AIAA Journal

AIAA JOURNAL
Vol. 63, No. 10, October 2025

Estimation of Rotor Blade Loading Distribution from Slipstream Velocity Measurements

Jatinder Goyal* and Tomas Sinnige†
Delft University of Technology, 2629 HS Delft, The Netherlands
Francesco Avallone‡
Polytechnic University of Turin, 10129 Turin, Italy
and
Carlos Ferreira§
Delft University of Technology, 2629 HS Delft, The Netherlands

https://doi.org/10.2514/1.J064736

Accurately determining experimental blade loading distributions is crucial for analyzing rotor performance but challenging due to the limitations of conventional measurement techniques. This paper presents a so-called *wake-informed lifting line* model that estimates blade loading distributions from phase-locked velocity measurements in the slipstream, eliminating the need for blade instrumentation. The model is evaluated against computational fluid dynamics (CFD) simulations under both attached and separated flow conditions. For the attached flow condition, the model achieves excellent agreement with CFD, with errors in the peak value of thrust distribution below 1%. In the separated flow condition, the model captures radial gradients and the shape of the thrust distribution but exhibits discrepancies in absolute values, with a 10% error in the peak value. These differences arise from the inherent limitations of the potential flow model, the increased significance of drag, and the heightened influence of the spinner's presence in separated flows. Incorporating profile drag through external polar data improves the model prediction, reducing the error to 4%. The model cannot reliably predict power distributions without external polar data for both attached and separated flows due to the crucial role of drag in the torque direction. The application of the model to experimental flowfield data shows a performance similar to that of the validation case. Therefore, the wake-informed lifting line model offers a promising approach for obtaining experimental blade loading distributions, overcoming the limitations of traditional methods.

Nomenclature

a_x	=	axial induction; $(V_x - V_\infty)/V_\infty$
B	=	number of propeller blades
C_T	=	propeller thrust coefficient; $T/\rho_\infty n^2 D^4$
c	=	section chord, m
c_d	=	sectional drag coefficient; $D'/q_\infty c$
c_l	=	sectional lift coefficient; $L'/q_\infty c$
c_o	=	speed of sound in dry air at 15°C, m/s
c_p	=	sectional power coefficient; $P'/\rho_\infty n^3 D^4$
c_t	=	sectional thrust coefficient; $T'/\rho_\infty n^2 D^3$
D	=	propeller diameter, m
J	=	propeller advance ratio; V_∞/nD
L'	=	sectional lift force, N/m
M	=	Mach number; V/c_o
M_{ht}	=	helicoidal tip Mach number; $\sqrt{M_\infty^2 + M_{\text{tip}}^2}$
M_{tip}	=	tip rotational Mach number; $\Omega R/c_o$
n	=	propeller rotation speed, Hz
P	=	propeller power, W
p	=	static pressure, Pa
q	=	dynamic pressure; $p(1 + ((\gamma-1)/2)M^2)^{\gamma/(\gamma-1)} - p$, Pa
R	=	propeller radius, m
Re_c	=	Reynolds number based on chord of the propeller blade; $\rho_\infty V_{\text{eff}} c/\mu_\infty$
r	=	radial coordinate, m
T	=	propeller thrust, N
T_C	=	propeller thrust coefficient based on freestream dynamic pressure; $T/\rho_\infty V_\infty^2 D^2$
t	=	section thickness, m
V	=	velocity, m/s
$\boldsymbol{V}_{\text{ind},i}^{\text{Helix}}$	=	velocity vector induced by the helical wake system at control point i
$\boldsymbol{V}_{\text{ind},i}^{\text{Slipstream}}$	=	velocity vector from input slipstream data at control point i
x	=	axial coordinate, m
α	=	angle of attack, deg
$\beta_{0.7R}$	=	blade pitch angle at 70% of the radius, deg
Γ	=	bound circulation, m^2/s
Γ^*	=	non-dimensional bound circulation, $\Gamma/V_\infty D$
γ	=	heat capacity ratio of dry air at 15°C
ΔC_T	=	error in propeller thrust coefficient
μ	=	dynamic viscosity of dry air at 15°C, $(\text{N}\cdot\text{s})/\text{m}^2$
ρ	=	air density, kg/m^3
ϕ	=	azimuthal position, deg
φ	=	inflow angle, deg
Ω	=	rotational speed; $2\pi n$, rad/s
$\boldsymbol{\omega}_t$	=	out-of-plane vorticity, 1/s
$\boldsymbol{\omega}_t^*$	=	nondimensional out-of-plane vorticity; $\boldsymbol{\omega}_t D/V_\infty$

Subscripts

∞	=	freestream
eff	=	combination of axial and rotational components

Received 13 August 2024; accepted for publication 2 March 2025; published online 2 May 2025.

*Ph.D. Candidate, Wind Energy Section, Faculty of Aerospace Engineering, Kluyverweg 1; j.goyal@tudelft.nl.
†Assistant Professor, Flight Performance and Propulsion Section, Faculty of Aerospace Engineering; t.sinnige@tudelft.nl.
‡Full Professor, Department of Mechanical and Aerospace Engineering, Corso Duca degli Abruzzi 24; francesco.avallone@polito.it.
§Full Professor, Wind Energy Section, Faculty of Aerospace Engineering; c.j.simaoferreira@tudelft.nl.

D = drag force contribution
L = lift force contribution
x = along the axial direction

Superscript

$'$ = per unit span

I. Introduction

ROTORS such as propellers and wind turbines are used in diverse applications, from aircraft propulsion to renewable energy generation. Understanding their aerodynamic and aeroacoustic performance is essential for design optimization and efficiency improvements. Traditionally, a combination of experimental measurements and numerical simulations is employed to gain insights into the aerodynamics of different designs. Experiments are often necessary to validate numerical simulations and to conduct parameter sweeps to evaluate the performance of a design under different conditions. However, certain performance quantities, such as blade loading distributions, are particularly challenging to measure accurately in experiments.

Blade loading distributions are essential for assessing the aerodynamic and aeroacoustic performance of rotor designs. Conventionally, obtaining blade loading data directly from experiments requires the use of intrusive measurement techniques, involving the installation of complex and costly surface pressure sensors on blade surfaces [2,3]. These sensors typically offer low spatial resolution due to several factors: their size relative to the thin blades of scaled models, the high cost of individual sensors, and the expense of high-bandwidth data transfer systems needed to transmit data from the rotating to the stationary domain [4]. These challenges are further amplified when dealing with off-the-shelf rotors, where customization of the rotor blades to accommodate pressure sensors is impractical. Additionally, limited information about the geometry of off-the-shelf rotors often necessitates three-dimensional (3D) scanning before numerical simulations can be performed, complicating the characterization of commercially available rotors.

Alternatively, multihole probes can be placed directly behind the blades to estimate total loads using momentum-based analysis techniques. However, accurately tracing these loads back to their exact radial origin on the rotor blades is not feasible, and measurements may be affected by viscous phenomena in the slipstream. Nonintrusive techniques, such as particle image velocimetry (PIV), encounter similar challenges. Although it is possible to reconstruct the pressure distribution around a blade segment using the stereoscopic velocity field obtained through PIV [5], this method encounters difficulties with optical access and increased uncertainty near the blade surface, potentially leading to significant inaccuracies in the reconstructed blade loading [6,7].

Previous work by Haans et al. [8] proposed a lifting line method to estimate local flow conditions at the blade and blade loads using wake measurements. They reconstructed the wake geometry assuming the trailing vorticity sheet rolls up into tip and root vortices at the boundary of the very near ($0 \leq x/R \leq 0.15$) and the near wake ($0.15 < x/R \leq 1$) regions. Subsequently, they solved for the unknown bound circulation based on velocities obtained from wake measurements, employing Kelvin's circulation theorem and the Biot–Savart law. Although this approach demonstrated potential, its application was limited to a simplified rotor blade geometry consisting of a NACA0012 airfoil without twist or taper and was primarily tested in wind turbine conditions. These conditions differ significantly from those encountered by aircraft propellers, particularly in terms of tip speed ratio (advance ratio). Additionally, their study lacked comprehensive validation, as it only compared local angles of attack derived from the potential flow method with experimentally estimated values.

In the present paper, the method proposed by Haans et al. has been extended. Although the theoretical formulation remains unchanged, the wake reconstruction methodology has been updated; the trailing vorticity sheet maintains its path and does not roll up into the tip and root vortices. This modification allows accounting for the variations in convective velocity along the radial direction. Furthermore, it has been adapted for application to propellers, with a focus on evaluating its effectiveness in estimating blade loading distributions directly from wake measurements under both attached and separated flow conditions.

The method in the current paper is referred to as the "wake-informed lifting line" model and is used in combination with phase-locked slipstream data containing all three velocity components. The method is first thoroughly validated using computational fluid dynamics (CFD) data, where both phase-locked data and computed blade-loading distributions are available. After validation, the model is applied to experimental data to assess its efficacy in practical scenarios. The wake-informed lifting line (LL) model presents a promising approach for estimating blade loading distributions directly from wake measurements, even in the absence of detailed rotor blade geometry.

II. Propeller Geometry and Operating Conditions

This study uses the three-bladed variant of the TUD-XPROP propeller to assess the capabilities of the wake-informed LL model. The propeller is a scaled-down version of a design used in previous-generation regional turboprop aircraft, with a diameter of 0.4064 m and a hub diameter of 0.092 m. The propeller can be seen in Fig. 1a along with its geometry parameters in Fig. 1b.

To test the capabilities of the wake-informed LL model, two operating conditions were selected, as detailed in Table 1. The first condition represents an attached flow scenario, characterized by positive thrust at an advance ratio J of 0.60 and a pitch angle $\beta_{0.7R}$ of 15 deg. The second condition represents a separated flow

a) Isolated propeller with three blades installed on a sting

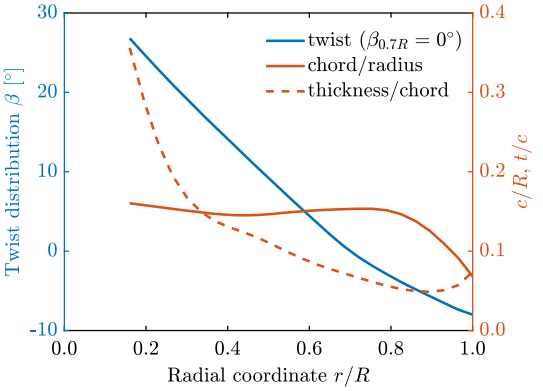

b) Propeller blade geometry at $\beta_{0.7R} = 0°$

Fig. 1 Propeller setup in the wind tunnel and geometry.

Table 1 Operating conditions used in this study

Case	T_C[a]	J	$\beta_{0.7R}$	V_∞, m/s	n, Hz	M_{ht}	max Re_c
$T > 0$	+0.1176	0.60	15°	30	123.03	0.47	3.5×10^5
$T < 0$	−0.1073	1.10	15°	30	67.11	0.27	2.0×10^5

[a]Measured in experiments [10] and corrected for wind-tunnel boundary interference.

scenario, characterized by negative thrust of comparable magnitude to the positive thrust case, with the propeller operating at $J = 1.10$ (close to the maximum power output point) and $\beta_{0.7R} = 15°$. The selection of these conditions is further supported by the availability of existing data. The Reynolds-averaged Navier–Stokes (RANS) simulations data from the authors' previous work [9] are used for model validation, while experimental data by Nederlof et al. [10] provide a real-world test case for the application of the wake-informed lifting-line model.

III. Lifting Line Models

This section provides a brief description of the conventional LL model. Subsequently, the theory of the wake-informed LL model is presented. Lastly, an additional way of solving the LL model, referred to as the "load-informed LL" model, is explained and is used as an intermediary validation tool in subsequent analyses.

A. Conventional Lifting Line Model

Conventionally, a lifting-line analysis of a rotor is performed to compute rotor performance based on prescribed blade geometry and airfoil polar data, with the rotor wake typically modeled as an incompressible, inviscid vortex system of fixed shape [11]. The strength of the shed vortices from the rotor corresponds to the spanwise gradient in bound vortex strength as per Kelvin's theorem, and the velocity induced by these vortices at any point on the rotor blade is calculated using the classical Biot–Savart law. For a given wake geometry and bound circulation strength, the induced velocity at the rotor blade can be calculated, which in turn can be used to determine the angle of attack at each blade section. To compute the resulting local lift and drag coefficients, polar data for different blade sections are required from an external source, which further requires knowledge of blade section geometry. This whole process is iterated until a converged solution is obtained, as shown in Fig. 2a. However, the conventional LL approach is applicable only to rotors with known geometries, and its accuracy is inherently limited by the precision of the polar data and prescribed wake shape.

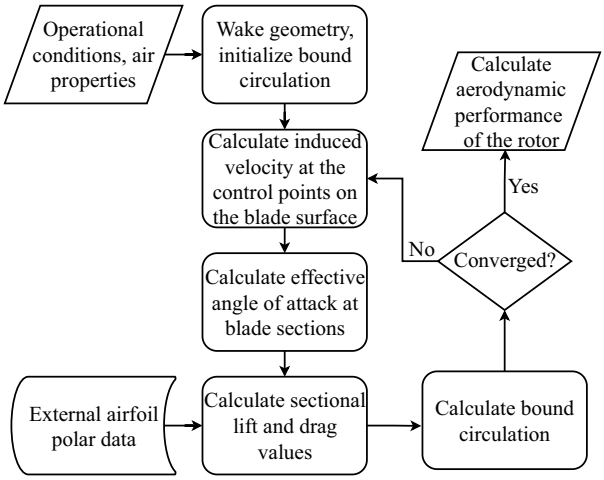

a) Conventional prescribed-wake lifting line

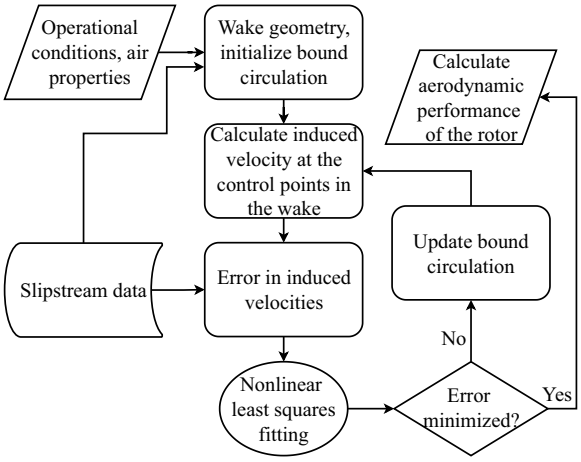

b) Wake-informed lifting line

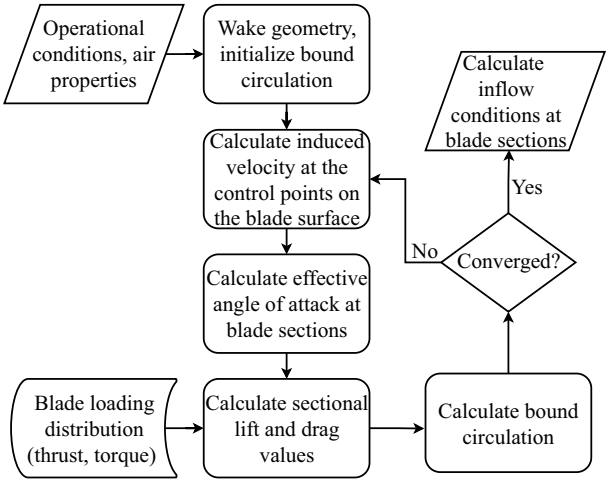

c) Load-informed lifting line

Fig. 2 Computational procedure to solve the conventional prescribed-wake lifting line, wake-informed lifting line, and load-informed lifting line models.

B. Wake-Informed Lifting Line Model[¶]

The wake-informed LL model is a modification of the conventional prescribed wake LL model that partially eliminates the need for airfoil polar data and blade section geometry to determine blade loading distributions. Instead, it uses the information available from input slipstream data, including the blade wake and tip vortex locations, as well as the induced velocity vectors to estimate the bound circulation.

In this model, the process begins by constructing a wake vortex system based on the blade wake and tip vortex locations identified in the slipstream data. An initial guess of the bound circulation is used to calculate the resulting induced velocities at prescribed locations in the slipstream, referred to as "control points." These control points are strategically positioned where the induced velocity vectors are available from the input slipstream data, avoiding regions dominated by viscous effects, such as the boundary layer of the nacelle. The bound circulation is then iteratively adjusted using nonlinear least-squares fitting to minimize the root sum square of the errors between the velocity vectors induced by the wake vortex system and the induced velocity vectors obtained from the input slipstream data at the control points. The trust-region-reflective (gradient-based) algorithm [12,13] was used for this optimization, though alternative algorithms could also be used. A detailed description of each step in setting up the model is provided in Sec. IV.

Once the fitting process converges, the resulting bound circulation distribution is used to compute the induced velocities at the blade sections, similar to the conventional LL model. However, it is important to note that the wake-informed LL model does not calculate the profile drag component without supplementary polar data; it only determines the lift component of the blade loading distribution. The computational procedure for the wake-informed LL model is shown in Fig. 2b.

C. Load-Informed Lifting Line Model

To enable a more direct comparison between the wake-informed LL model and validation data, this study also employs an alternative formulation, referred to as the "load-informed lifting line" model. Unlike conventional LL models, where the blade loading distributions (thrust and torque distributions) are obtained as outputs, this model takes the blade loading distributions as input from an external source and decomposes them into their corresponding lift and drag components.

The load-informed LL model serves two purposes. First, by decomposing the thrust and torque distributions obtained from validation data into lift and profile drag components, it enables a more fair comparison between the wake-informed LL model and validation data. This is particularly important because the wake-informed LL model, as mentioned in Sec. III.B, does not provide the profile drag component. This decomposition also provides insight into the significance of the profile drag component for thrust and torque distributions.

Second, the load-informed LL model provides the equivalent potential flow solution for the given blade loading distribution. The induced velocities in the slipstream, calculated using the load-informed LL model, serve as a benchmark for evaluating the wake-informed LL model. Assuming the fundamental assumptions of LL theory hold, the wake-informed LL model should theoretically converge to the load-informed LL solution. Significant discrepancies between the load-informed LL and wake-informed LL solutions would indicate that potential flow solutions obtained using LL models cannot reconcile the given combination of blade loading and the induced velocities in the slipstream for a given operating condition, or in other words, the fundamental assumptions of the LL models are not representative of the given operating condition.

To achieve this, the computational procedure for the load-informed LL model begins with a predefined helical wake structure and an initial guess for the bound circulation. The model then calculates the induced velocities at the quarter-chord points of the blade sections, which are then used to determine the local inflow angles $\varphi(r)$. Using Eqs. (1) and (2) and the input blade loading distributions, the corresponding lift and drag forces are computed:

$$T'(r) = L'(r)\cos\varphi(r) - D'(r)\sin\varphi(r) \tag{1}$$

$$Q'(r) = (L'(r)\sin\varphi(r) + D'(r)\cos\varphi(r))r \tag{2}$$

The calculated lift is subsequently employed to update the bound circulation. This iterative process continues until a converged bound circulation is obtained. The computational procedure is shown in Fig. 2c.

To ensure consistency, all load-informed LL solutions in this study use the same helical wake system as the wake-informed LL model, thereby avoiding discrepancies due to variations in wake geometry.

IV. Setup of Wake-Informed Lifting Line Model

This section details the problem setup for the wake-informed LL model. It begins with a description of the required slipstream data for the model, followed by the procedure for identifying blade wake and tip vortex structures using these input data. Next, the methodology for setting up the helical wake system and choosing the control points is described. Then, the objective function minimized to obtain the solution is described. Finally, the postprocessing of the results is discussed.

A. Slipstream Data

The setup of the wake-informed LL model requires phase-locked slipstream data. Although the axial velocity component is essential for the wake-informed LL model and must be available in the slipstream data, the inclusion of the radial and tangential velocity components, when available, contributes to achieving a more accurate and representative solution.

For the rest of this section, slipstream data derived from steady RANS (SRANS) simulations from the authors' previous work [9] are used as examples. These data are also employed later for validation in Sec. V. A brief description of the simulation setup is provided in Appendix A. The slipstream data consist of phase-locked velocity vectors calculated in a plane behind the propeller blade, extending to approximately $1.2R$ in both axial and radial directions. This measurement plane aligns with the dimensions and location of the plane employed in PIV experiments conducted by Nederlof et al. [10] for the same propeller. These PIV measurements will be used later for a real-world test case of the model in Sec. VI. The input slipstream data from the RANS simulations include all three velocity components. The availability of the axial and radial velocity components from RANS simulations enabled the identification of the blade wake and tip vortex shapes and locations using the out-of-plane vorticity field.

Figure 3 shows the corresponding phase-locked out-of-plane vorticity field for both attached and separated flow conditions. For the attached flow condition (Fig. 3a), two blade wakes are observed in the specified plane. In contrast, for the separated flow condition (Fig. 3b), only one blade wake is visible. This difference results from the lower advance ratio in the attached flow condition compared to the separated flow condition. In the attached flow condition, the blade wakes show the expected shape, with the midboard part of the blade wake convecting faster than the wake from the tip and root regions. Conversely, in the separated flow condition, the blade wake originating from the inboard part of the blades convects slower than the outboard region due to higher negative loading in the inboard region.

B. Identifying Shape and Location of Blade Wake and Tip Vortex

Identifying blade wake and tip vortex locations is crucial for setting up the vortex wake system for the wake-informed LL model. In this study, these features are determined using vorticity fields. However, if vorticity fields are unavailable due to the absence of

[¶]The source code of the wake-informed LL model used in this study can be found on 4TU.ResearchData repository [1].

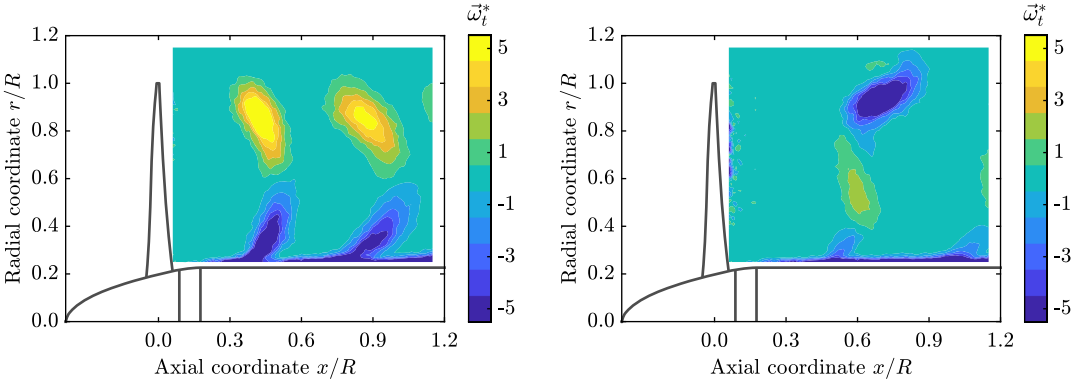

a) Attached flow condition ($J = 0.60, T > 0$) **b) Separated flow condition ($J = 1.10, T < 0$)**

Fig. 3 Phase-locked nondimensional out-of-plane vorticity component ω_t^* obtained from RANS simulations.

radial velocity data, an alternative approach is to use the axial velocity gradient in the axial direction ($\partial V_x/\partial x$) as a substitute, as discussed in Appendix B. The procedure followed in this study to identify these features using the vorticity field is detailed in the following:

1) A Gaussian filter $\mathcal{G}(\boldsymbol{r})$ is applied to the input $\boldsymbol{\omega}_t^*$ values to mitigate noise in the measurement plane, which is especially important when dealing with experimental data.

2) A vorticity $\boldsymbol{\omega}_t^*$ threshold is defined to identify regions where vorticity values exceed the threshold magnitude. These regions are expected to correspond to the desired features, such as blade wakes and tip vortices. However, the filtering process may also capture unwanted features, such as the boundary layer of the nacelle. In this study, a threshold of $\boldsymbol{\omega}_t^* < -3.5 \vee \boldsymbol{\omega}_t^* > 3.5$ was applied for the attached flow case, while a threshold of $\boldsymbol{\omega}_t^* < -1.5 \vee \boldsymbol{\omega}_t^* > 0.6$ was used for the separated flow case.

3) Additional constraints, informed by the vorticity field visualization (Fig. 3), are defined to exclude regions associated with boundary layers and other extraneous features, such as support struts in experimental setups. These constraints may be applied to the axial coordinate, radial coordinate, vorticity values, or a combination of these parameters.

4) In case of multiple wakes in the measurement plane, the remaining measurement points are divided into distinct bins. These bins are defined based on the minimum and maximum axial locations for each blade wake and tip vortex, as informed by the vorticity field visualization (Fig. 3). For instance, for the attached flow condition ($J = 0.60$), two bins were defined: the first bin corresponds to $x/R \leq 0.60$, and the second bin corresponds to $x/R > 0.60$. No binning was necessary for the separated flow condition, as only one blade wake was present in the measurement plane.

5) A polynomial curve is fitted along the radial direction through the remaining points in each bin to obtain the shape of the blade wake in the specified plane. The initial polynomial orders were determined by minimizing the root mean square errors. Subsequently, terms with a probability greater than 5% of having a nonzero coefficient due to random error were eliminated to obtain the final polynomial curve [14]. A practical approach to validate the identified shape is to overlay it on the $\boldsymbol{\omega}_t^*$ plot (Fig. 4). This step helps assess whether the determined shape is physically realistic, particularly near the nacelle where input slipstream data may be sparse or unavailable. In this study, third-order and sixth-order polynomials were used for attached and separated flow conditions, respectively, for the input RANS data.

Figure 4 shows the resulting Gaussian-filtered vorticity field, overlaid with red points where the vorticity magnitude exceeds the threshold values. Additionally, the final polynomial curves, fitted through these high-vorticity points, are also displayed. These polynomial curves extend from the nacelle ($r/R = 0.24$) to the blade tip ($r/R = 1.0$).

C. Setup of Helical Wake System

For simplicity, this study assumes no wake contraction when setting up the helical wake system. However, when necessary, contraction can be accounted for using Eq. (3), originally derived by Veldhuis [15],

$$\frac{r_x}{r} = \sqrt{\frac{1+a}{1+a\left(1+\frac{x}{\sqrt{r^2+x^2}}\right)}} \tag{3}$$

where r_x is the contracted radius of the annulus (jn meters) at an axial distance of x downstream of the propeller (in meters), r is the radius of the annulus at the propeller disk (in meters), and a is the average axial induction of the given annulus at the rotor disk.

The helical wake system is defined by calculating the convection velocity at each radial station. The convection velocity of each blade wake is determined by dividing the axial distance between

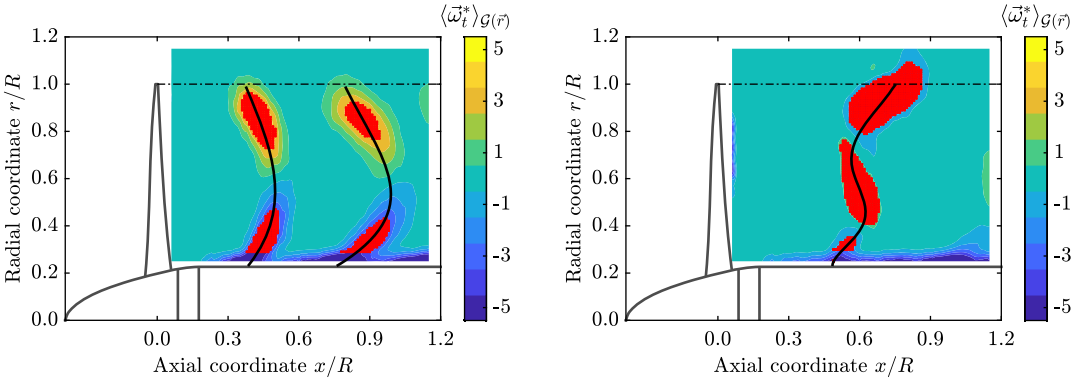

a) Attached flow condition ($J = 0.60, T > 0$) **b) Separated flow condition ($J = 1.10, T < 0$)**

Fig. 4 Identified shape of blade wakes and tip vortices.

consecutive wakes by the time interval between their passage through the measurement plane ($1/nB$). For the first blade wake, the axial distance is measured from the propeller plane, taking into account the phase angle of the measurement plane relative to the reference propeller blade (0 deg in this study). In cases where multiple wake structures are detected in the slipstream data, the convection velocity of the blade wake varies between consecutive wakes; that is, the convection velocity between the propeller plane and the first wake differs from the convection velocity between the first and second wakes, and so on. The convection velocity of the wake beyond the last wake structure is assumed to be the same as that calculated between the second-to-last and last wake structures.

The resulting helical wake systems can be seen in Figs. 5a and 5c for the attached and separated flow conditions, respectively, along with the zoomed-in views in Figs. 5b and 5d. In the setup, the length of the wake is defined to be $5R$ for the vortex line shed from the blade tip based on sensitivity studies investigating the influence of wake length on bound circulation. However, due to the variation in convection velocity with radial location, the resulting helical wake system stretches out for both conditions. In the attached flow condition, the blade wake convects at a higher speed in the midboard region than in the root and tip regions, resulting in a wake extending up to approximately $6R$ in the midboard area. In contrast, the convection speed is highest at the blade tip in the separated flow condition. Therefore, the wake extends between $4R$ and $5R$ depending on the radial location for the separated flow condition in Fig. 5c.

1. *Radial Discretization*

Defining the vortex wake system requires selecting an appropriate number of radial stations from which vortex lines emanate and convect in the slipstream. A sensitivity study was conducted for various radial discretizations, with the resulting nondimensionalized bound circulations shown in Fig. 6. For all the radial discretizations, the two innermost vortex lines were consistently located at $r/R = 0.24$ and $r/R = 0.30$. The first vortex line corresponds to the root vortex and is determined by the nacelle diameter, while the second one was selected to ensure that the vortex line intersects the input measurement plane. This avoids placing multiple vortex lines at

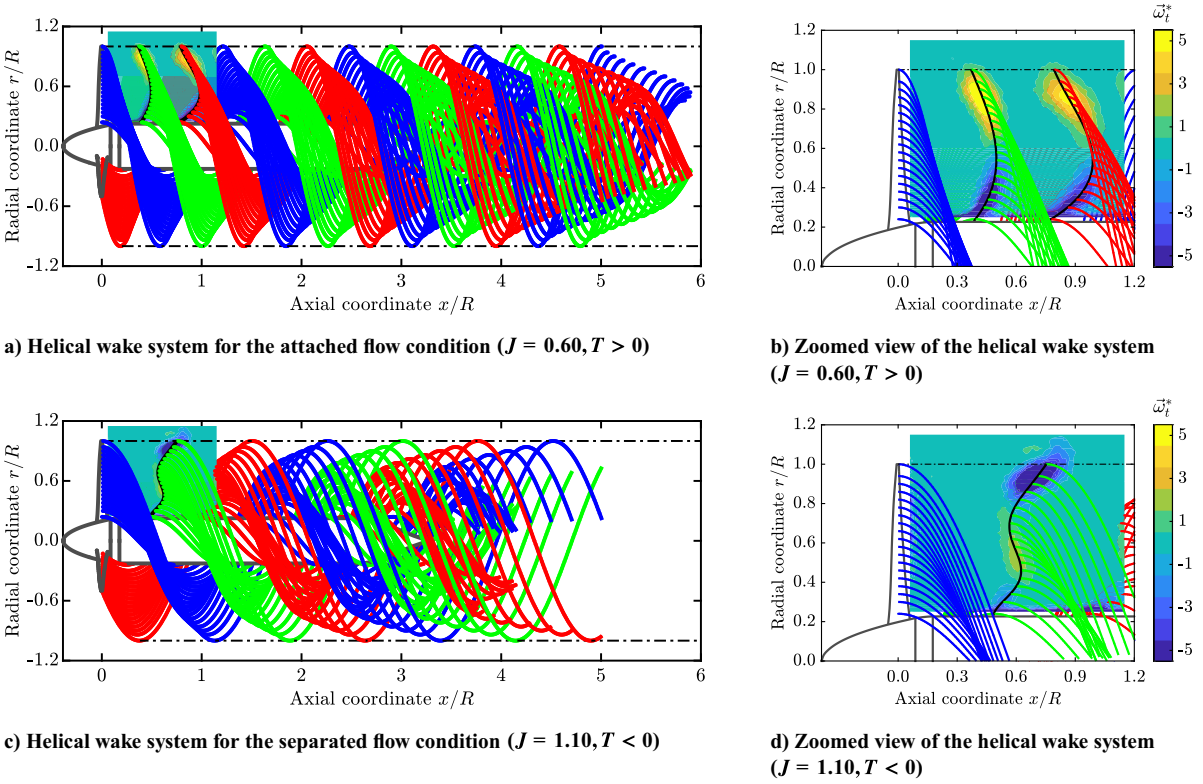

a) Helical wake system for the attached flow condition ($J = 0.60, T > 0$)

b) Zoomed view of the helical wake system ($J = 0.60, T > 0$)

c) Helical wake system for the separated flow condition ($J = 1.10, T < 0$)

d) Zoomed view of the helical wake system ($J = 1.10, T < 0$)

Fig. 5 Setup of helical wake geometry for the wake-informed lifting line method.

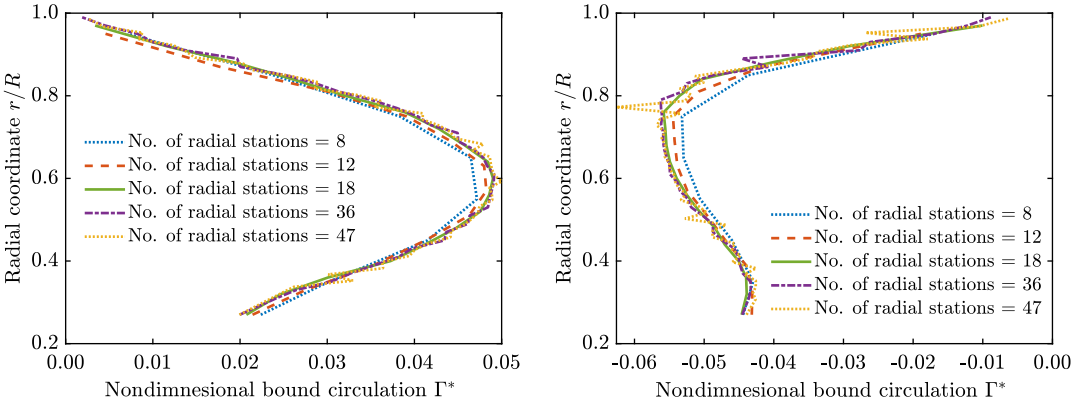

a) Attached flow condition ($J = 0.60, T > 0$)

b) Separated flow condition ($J = 1.10, T < 0$)

Fig. 6 Effect of radial discretization on the non-dimensionalized bound circulation for the wake-informed lifting line method.

radial locations lacking input velocity data, which could otherwise introduce high uncertainty. Without this restriction, vortex lines might cluster too closely relative to their nearest control point, making the solution overly sensitive to the placement of control points. This sensitivity arises because induced velocities, as per Biot–Savart's law, are inversely proportional to the square of the distance between the vortex line and the control point.

The impact of such clustering is evident in the finest discretization (47 radial stations) considered in the sensitivity study, where oscillatory behavior is observed, particularly for the attached flow case (Fig. 6a). Similar oscillations were observed for the second-finest discretization (36 radial stations) for both attached and separated flow cases. Conversely, the coarsest resolution (eight radial stations) leads to an underprediction of the peak value of the circulation magnitude. Therefore, to balance accuracy and stability, a sensitivity analysis is recommended for each case to identify the optimal radial resolution. For this study, 18 radial stations were chosen for further sensitivity studies conducted in Sec. IV.D and validation of the model against RANS data for both attached and separated flow conditions.

D. Setup of Control Points

After defining the helical wake system, the next step is to set up the control points, which are used to inform the nonlinear least-squares fitting to obtain the bound circulation on the propeller blades. The positions of the control points need to be chosen carefully as the fitting process aims to minimize the root sum square of the errors between the velocities induced by the helical system and the input slipstream data. The following procedure is employed to position the control points:

1) Start by populating the measurement plane with a certain number of random points. In this study, 1000 points were used for this process.

2) Remove points that are too close to the propeller blades to avoid areas influenced by the blade thickness effect, which is not accounted for by LL models. Based on the sensitivity study presented in Sec. IV.D.2, for the attached flow condition, points within a threshold distance of $x/R < 0.20$ from the propeller blades were excluded, while for the separated flow condition, a threshold distance of $x/R < 0.30$ was used. This can be seen in Fig. 7.

3) To ensure numerical stability, the control points within a specified axial distance from the identified blade wake (from previous steps) are excluded to avoid having points too close to the helical element that can result in destabilizing the solution. In this study, this tolerance was chosen to be $x/R < 0.010$ based on the sensitivity study presented in Sec. IV.D.3, and the affected regions are indicated with dashed blade lines in Fig. 7.

4) Finally, remove control points located within the boundary layer of the nacelle based on their axial or radial coordinates or the out-of-plane vorticity values, as potential flow methods cannot simulate boundary layer effects.

Theoretically, control points located within high-vorticity regions near the blade wakes and tip vortices should be removed, as LL models do not explicitly simulate viscous effects. However, viscous effects still influence blade loading distributions in real-world scenarios. Therefore, control points in high-vorticity regions are retained to derive a nonlinear least-squares solution that aligns with the blade loading distributions implied by the input slipstream data.

This process resulted in approximately 800 control points for the present study. An example of the resulting control point distribution is shown in Fig. 7. Alternatively, one could have first masked the domain and then distributed a set number of random points across the remaining measurement plane.

1. *Statistical Convergence*

The solution is expected to be sensitive to the choice of the control points. To mitigate this sensitivity and achieve statistical convergence, the model needs to be solved multiple times using a randomly distributed set of control points in each iteration, with the bound circulation averaged over these iterations.

Figure 8 presents the averaged bound circulations obtained from the wake-informed LL model for different numbers of randomly distributed control point sets under both attached and separated flow conditions. After just 10 passes, the solution exhibited less than 1% deviation from the 100-pass result across most of the blade span, excluding the tip region. Therefore, the additional passes beyond 10 have minimal impact on the converged bound circulation. However, to ensure statistical robustness and establish a 95% confidence interval, the 100-pass solution was used in this study. The corresponding confidence interval is shown as a shaded region around the mean solution in the figure.

2. *Sensitivity to Threshold Distance from Propeller Blade*

Figure 9 shows the sensitivity of the nondimensionalized bound circulations (after 10 passes) to the threshold distance from the propeller blade. Because the mean values were already shown to converge after 10 passes in the previous section, only 10 passes were used for this sensitivity study. The threshold distance was varied from $x/R < 0.06$, representing the axial location where the input slipstream data begins, to $x/R < 0.40$.

For the attached flow condition (Fig. 9a), increasing the threshold distance from $x/R < 0.06$ to $x/R < 0.20$ results in a 4.1% increase in the peak value of the bound circulation (using $x/R < 0.20$ as the reference). This change underlines the influence of the blade thickness effect in regions closer to the propeller. Beyond $x/R < 0.20$, further increases in the threshold distance lead to minimal variations in the bound circulation, with only a 0.7% change in the peak value.

For the separated flow condition (Fig. 9b), increasing the threshold distance from $x/R < 0.06$ to $x/R < 0.20$ leads to an 11.6% change in the peak value, again using $x/R < 0.20$ as the reference. A further increase in the threshold distance from $x/R < 0.20$ to $x/R < 0.30$ results in a 1.6% change, with negligible variations beyond $x/R < 0.30$. The higher threshold distance required for the separated flow condition, compared to the attached flow condition, is a result of flow separation around the blades. This separation

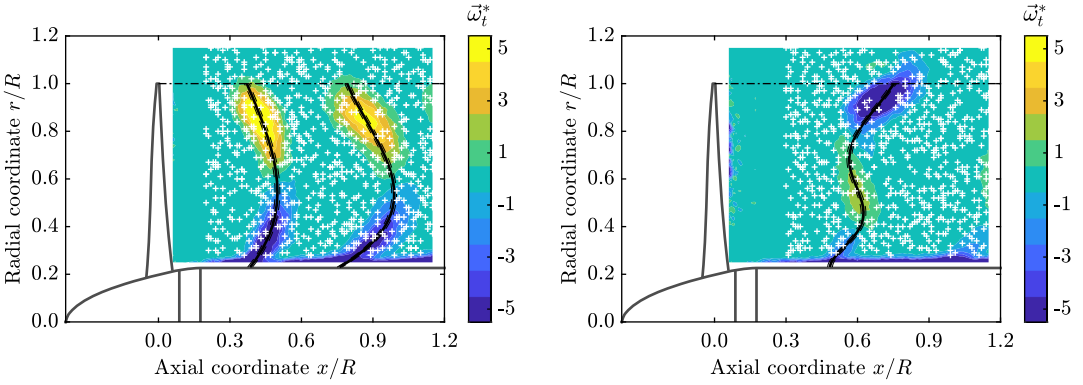

a) Attached flow condition ($J = 0.60, T > 0$) **b) Separated flow condition ($J = 1.10, T < 0$)**

Fig. 7 Setup of control points for the wake-informed lifting line method.

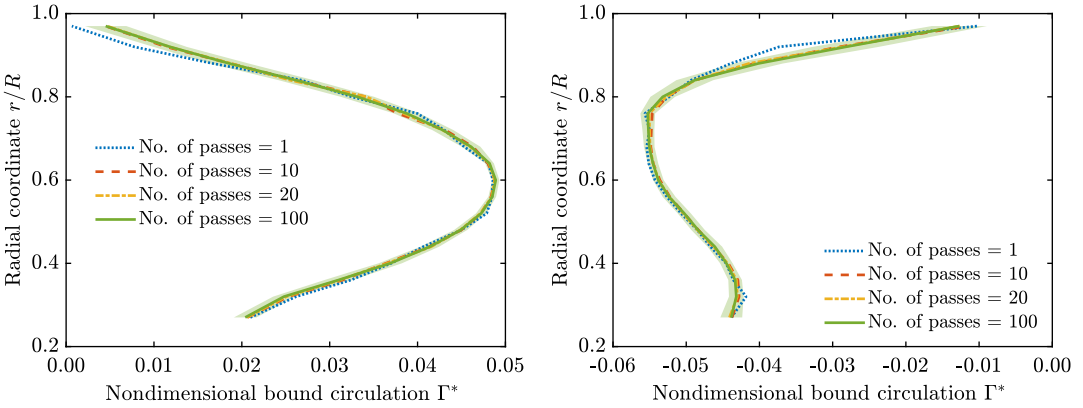

a) Attached flow condition ($J = 0.60, T > 0$) **b) Separated flow condition ($J = 1.10, T < 0$)**

Fig. 8 Statistical convergence of the wake-informed lifting line solution.

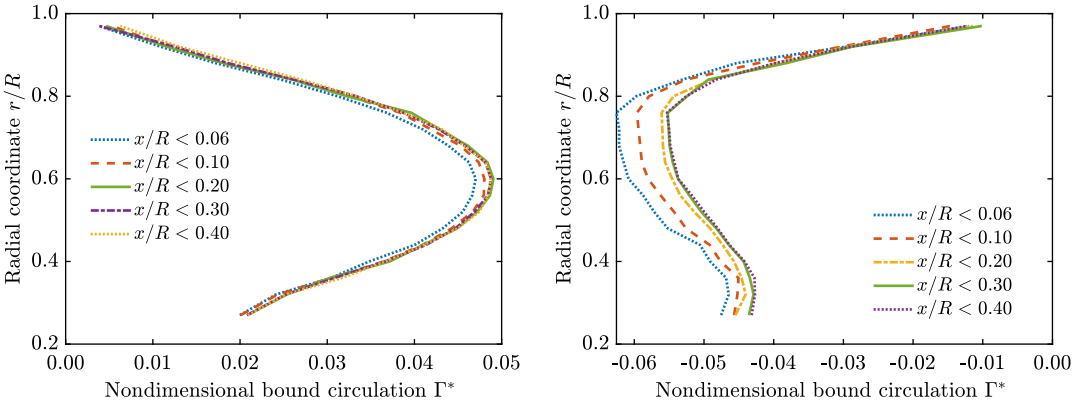

a) Attached flow condition ($J = 0.60, T > 0$) **b) Separated flow condition ($J = 1.10, T < 0$)**

Fig. 9 Sensitivity analysis of the wake-informed lifting line solution to the threshold distance from propeller blade.

effectively makes the blade thicker in the separated flow case than in the attached flow case.

Based on these observations, threshold distances of $x/R < 0.20$ and $x/R < 0.30$ were selected for the attached and separated flow conditions, respectively, to minimize the influence of the blade thickness effect on the wake-informed LL solution.

3. *Sensitivity to Threshold Distance from Wake Structures*

Figure 10 shows the sensitivity of the nondimensionalized bound circulations (after 10 passes) to the variations in the threshold distance from wake structures, ranging from $\Delta x/R < 0.005$ to $\Delta x/R < 0.030$. For the threshold distance of $\Delta x/R < 0.030$, the solution exhibits some fluctuations in the bound circulation, particularly for the attached flow condition. These fluctuations arise because the distance of the closest control point ($\Delta x/R = 0.030$) becomes comparable to the distance between adjacent vortex lines ($0.04R$) for the chosen radial discretization with 18 radial stations. The comparable distances make the solution overly sensitive to the placement of control points, as previously discussed in Sec. IV.C. Reducing the threshold distance results in a smoother solution for both attached and separated flow cases.

For the attached flow condition (Fig. 10a), reducing the threshold distance from $\Delta x/R < 0.030$ to $\Delta x/R < 0.010$ decreases the peak bound circulation by 2.6% (with $\Delta x/R < 0.010$ as the reference).

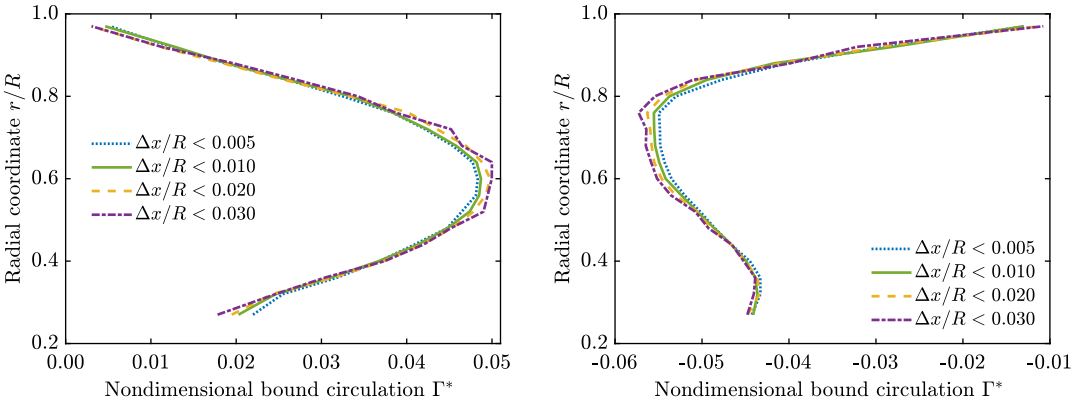

a) Attached flow condition ($J = 0.60, T > 0$) **b) Separated flow condition ($J = 1.10, T < 0$)**

Fig. 10 Sensitivity analysis of the wake-informed lifting line solution to the threshold distance from wake structures.

Further reducing the threshold to $\Delta x/R < 0.005$ results in negligible changes to the bound circulation distribution along the blade span, with a marginal decrease of 0.8% for the peak value. Similarly, for the separated flow condition (Fig. 10b), reducing the threshold distance from $\Delta x/R < 0.030$ to $\Delta x/R < 0.010$ decreases the peak value by 3.2%. A further reduction of the threshold distance to $\Delta x/R < 0.005$ results in minimal impact on the distribution and a 1% decrease in the peak value (relative to $\Delta x/R < 0.010$).

Based on these results, the threshold distance of $\Delta x/R < 0.010$ was deemed suitable for further analysis. This choice provides a smooth solution by avoiding the placement of control points too close to the wake structures, which could destabilize the solution due to the inverse-square dependence of induction on the distance between control points and wake structures.

E. Objective Function and Solution Algorithm

The bound circulation is determined by minimizing the root sum square of the errors between the velocity vectors induced by the helical wake system, as set up in Sec. IV.C, and the induced velocity vectors obtained from the input slipstream data at the control points. Mathematically, this can be expressed using Eq. (4),

$$\min_{\Gamma(r)} \sum_{i=1}^{N} \left\| \boldsymbol{V}_{\text{ind},i}^{\text{Helix}}(\Gamma) - \boldsymbol{V}_{\text{ind},i}^{\text{Slipstream}} \right\|^2 \tag{4}$$

where $\boldsymbol{V}_{\text{ind},i}^{\text{Helix}}(\Gamma)$ represents the velocity vector induced by the helical wake system at control point i and $\boldsymbol{V}_{\text{ind},i}^{\text{Slipstream}}$ is the corresponding velocity vector from the input slipstream data.

This minimization is performed using nonlinear least-squares fitting. This study employed the trust-region-reflective (gradient-based) algorithm [12,13] for the minimization, though other algorithms could also be used.

F. Postprocessing

The wake-informed LL model provides the converged bound circulation distribution along the blade span. This distribution, combined with the helical wake system, allows for the determination of all three components of the induced velocities at the quarter-chord point of each blade section and other desired locations. Using the induced velocities at the quarter-chord point of blade sections, the local inflow angle and local velocity vector at each blade section can be calculated. These parameters, along with the bound circulation, can be used to calculate the lift force contribution to thrust and torque as per Eqs. (5) and (6). Additionally, the local lift coefficient and angle of attack can be calculated using Eqs. (7) and (8), provided the chord and twist distributions along the blade span are known:

$$T_L'(r) = \rho_\infty V(r)\Gamma(r)\cos\varphi(r) \tag{5}$$

$$Q_L'(r) = \rho_\infty V(r)\Gamma(r)\sin\varphi(r)r \tag{6}$$

$$c_l(r) = \frac{2\Gamma(r)}{V(r)c(r)} \tag{7}$$

$$\alpha(r) = \beta(r) - \varphi(r) \tag{8}$$

To incorporate the missing drag force contribution in the thrust and torque equations (9) and (10), external polar data are required. In this study, the polar data were generated using RFOIL [16], which is a modification of the well-known two-dimensional-panel method XFOIL [17]. RFOIL was selected for its better lift and drag coefficient prediction in the poststall region [18]. Moreover, the quasi-three-dimensional model available in RFOIL was used to account for the influence of Coriolis and centrifugal forces on the boundary-layer characteristics of rotating airfoils [19,20]. To address compressibility and Reynolds number effects, polar data were generated at various Mach and Reynolds numbers for 24 radial stations using RFOIL:

$$T_D'(r) = -0.5\rho_\infty V^2(r)c(r)c_d(r)\sin\varphi(r) \tag{9}$$

$$Q_D'(r) = 0.5\rho_\infty V^2(r)c(r)c_d(r)\cos\varphi(r)r \tag{10}$$

These resulting polar data were interpolated with respect to radial position, local Reynolds number, and local Mach number based on the local effective velocity $V(r)$ and chord of the blade sections $c(r)$ to obtain the drag coefficient c_d. Interpolation with respect to radial position is necessary because the chosen radial discretization may not align with the stations for which the airfoil geometry and corresponding polar data are available. This interpolation was performed in two steps. First, the polar data were interpolated using Delaunay triangulation of the sample points to obtain the drag coefficient for each radial location and local Reynolds number across all input Mach numbers at a given lift coefficient $c_l(r)$ based on the solution from the wake-informed LL model. In the subsequent step, the resulting drag coefficient values were linearly interpolated to obtain the values at the specified local effective Mach number. A similar procedure was used to obtain the corresponding angle of attack values from the polar data, allowing for comparison with the angle of attack values derived from the wake-informed LL model.

V. Validation of Wake-Informed Lifting Line Model

In this section, the wake-informed LL method is validated by comparing its results with those obtained from RANS simulations, using the load-informed LL method as an intermediate tool for validation. The validation process begins with a comparison of axial induction in the slipstream, followed by an evaluation of blade loading distributions. Finally, the integrated thrust values obtained from the wake-informed LL model are compared against those from RANS simulations.

A. Axial Induction

Minimizing the root-sum-square error between induced velocity components from the wake-informed LL model and the input data does not necessarily result in identical induced velocities due to inherent limitations of LL models, such as their inability to account for viscous effects, blade thickness, and nacelle presence. Consequently, these differences serve as a measure of the solution's accuracy. This section compares axial inductions from the wake-informed LL model with input inductions from RANS data in the slipstream, starting with the attached flow condition, followed by the separated flow condition.

1. *Attached Flow Condition ($J = 0.60$)*

Figure 11 compares axial inductions obtained from RANS, load-informed LL, and wake-informed LL in the plane directly behind the propeller blade for the attached flow condition. Contour plots of axial induction for each method are shown in Figs. 11a–11c. The solid-black lines in these figures indicate the locations where the helical wake system of the LL models intersects the plane, also shown on top of the RANS data for reference. Additionally, Figs. 11d and 11e show the comparison of the axial induction along the radial and axial lines located at $x/R = 0.6$ and $r/R = 0.6$, respectively, with dashed black lines marking their locations in the contour plots. The comparison between the load-informed LL and wake-informed LL models (Figs. 11b–11e) shows negligible differences, confirming the validity of the assumptions inherent to the LL models for this operating condition.

The comparison of contour plots (Figs. 11a–11c) shows significant differences near the blade ($x/R < 0.20$) between both LL models and RANS simulations. This discrepancy is due to the inability of the LL models to replicate the thickness effect of the propeller blade, and as a result, the control points were removed from this region (Sec. IV.D). However, away from the blade ($x/R \geq 0.20$), all three methods show qualitative similarities. As LL models do not simulate the presence of a nacelle, differences compared to RANS data are apparent near the nacelle. This is further confirmed by the line plot at $x/R = 0.60$ in Fig. 11d, in

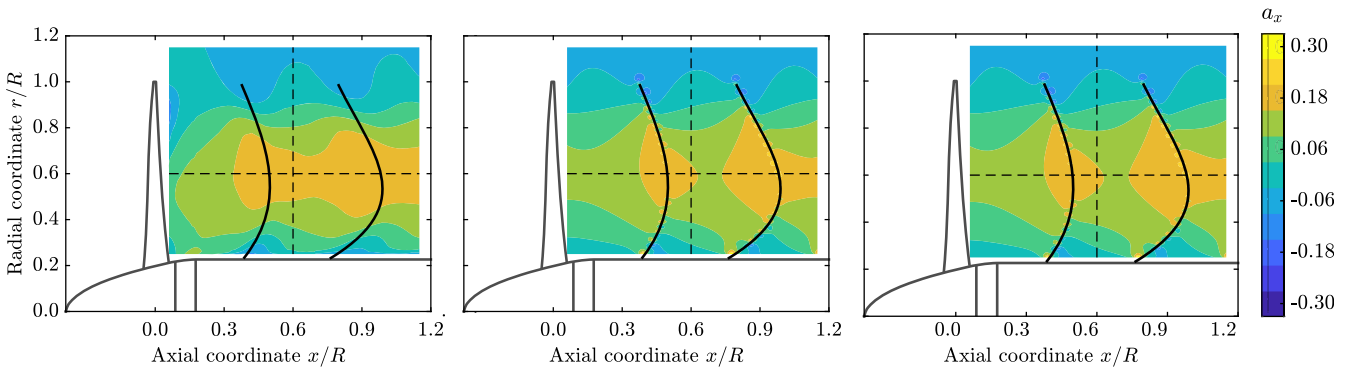

a) RANS **b) Load-informed LL** **c) Wake-informed LL**

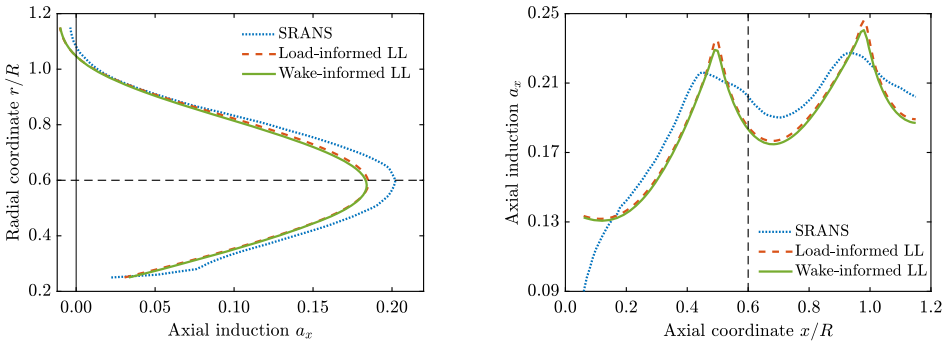

d) Comparison of axial induction along a radial line located at $x/R = 0.60$ **e) Comparison of axial induction along an axial line located at $r/R = 0.60$**

Fig. 11 Comparison of axial induction in the slipstream for the attached flow condition ($J = 0.60, T > 0$).

which the nacelle boundary layer is evident in the RANS data. Despite this limitation, both LL models show good agreement with RANS data except for the underprediction of the peak value of the induction near $r/R = 0.60$ by approximately 9%. This discrepancy is likely due to the omission of slipstream contraction in the LL models, as implemented in this study.

The comparison along the axial direction at $r/R = 0.60$ (Fig. 11e) shows a good qualitative agreement between LL models and RANS except near the blade ($x/R \leq 0.20$), as discussed earlier. LL models exhibit a sharp peak near blade wakes due to the inviscid flow assumption, while RANS data show a flattened peak due to viscous effects and numerical diffusion. Also, there is an apparent axial offset between the axial induction distributions obtained from RANS and LL models. This discrepancy is likely due to the blade wake (the position where the helical wake system cuts the measurement plane) being defined at a slightly different position in the LL models compared to its position in the RANS simulations.

Section V.B evaluates the impact of the observed differences between the wake-informed LL model and RANS on the predicted blade loading distributions.

2. *Separated Flow Condition ($J = 1.10$)*

Figure 12 compares axial inductions in the slipstream behind the propeller blade for the separated flow condition. The differences near the nacelle between RANS and LL models (Figs. 12a–12c) are again due to the inability of LL models to account for the presence of nacelle, confirmed by the radial line plot at $x/R = 0.90$ in Fig. 12d. However, away from the nacelle ($r/R > 0.40$), a qualitative agreement can be observed between the three methods, with differences of up to 21 and 30% observed for the wake-informed LL and load-informed LL models, respectively, within the range $0.4 \leq r/R \leq 0.9$, when compared to RANS data. Similar to the positive thrust case, the flowfield close to the propeller blades ($x/R < 0.30$) is significantly different due to the inability of the LL models to simulate thickness effects. These differences are evident in the axial line plot at $r/R = 0.60$ in Fig. 12e. However, away from the blade ($x/R \geq 0.30$), a qualitative agreement can be observed between the three methods, with a difference of up to 12% for wake-informed LL and up to 19% for load-informed LL as compared to RANS at the intersection of the blade wake with the specified plane (shown with solid-black line in contour plots). Because the wake-informed LL model uses RANS slipstream data as an objective function for the solution, it exhibits a lower error than the load-informed LL model.

Overall, higher discrepancies are observed for the separated flow condition between the wake-informed LL model and RANS data as compared to the attached flow condition. These increased differences suggest that the inherent assumptions of the wake-informed LL model, such as perfectly helical wake and inviscid flow assumptions, may not accurately represent this operating condition. This is further confirmed by the observed increased differences between the wake-informed LL and the load-informed LL models.

B. Blade Loading Distributions

This section evaluates the accuracy of the wake-informed LL model in predicting blade loading distributions. To this end, thrust and power distributions obtained from the wake-informed LL model are compared with those from RANS simulations. As a potential flow method, the wake-informed LL model inherently captures only lift force contributions (c_{t_L}, c_{p_L}) to thrust and power distributions Eq. (11) and requires external polar data for the estimation of the profile drag contributions (c_{t_D}, c_{p_D}):

$$c_t = c_{t_L} + c_{t_D}, \quad c_p = c_{p_L} + c_{p_D} \tag{11}$$

Although a direct comparison with RANS data is informative for practical applications, it is not suitable for a comprehensive model assessment. To address this, two types of comparisons are conducted:

1) For evaluation of the importance of drag force contribution to blade loads: The load-informed LL model is used to decompose the blade loading distribution from RANS into its lift and profile drag components. Comparing the lift contribution from the load-informed

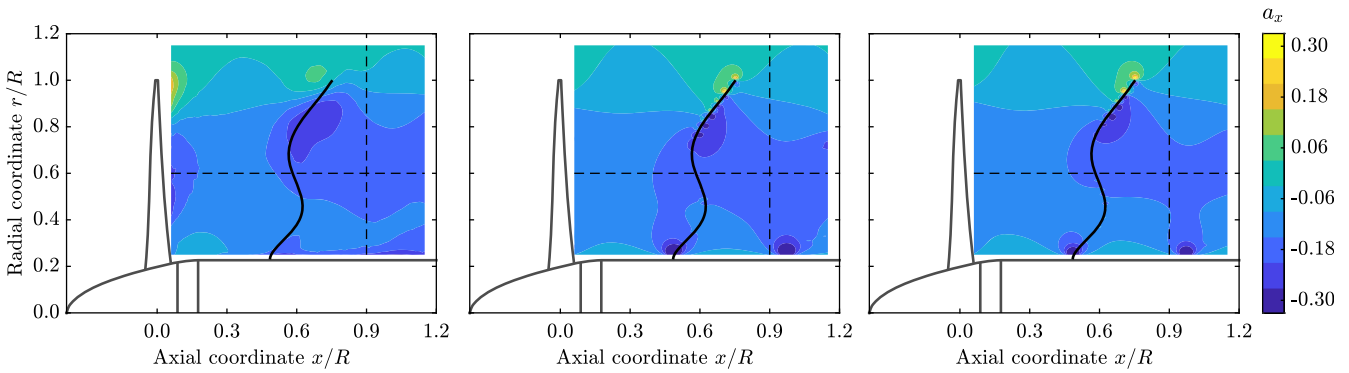

a) RANS b) Load-informed LL c) Wake-informed LL

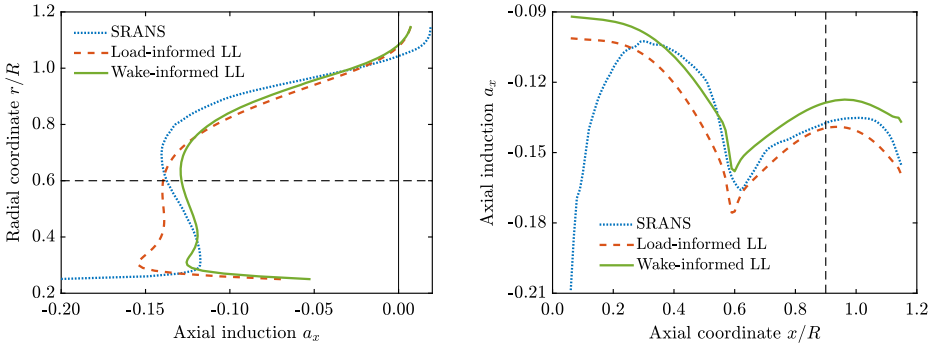

d) $x/R = 0.90$ e) $r/R = 0.60$

Fig. 12 Comparison of axial induction in the slipstream for the separated flow condition ($J = 1.10, T < 0$).

LL model with the total blade loading from RANS provides insights into the importance of the drag contribution for the given blade loading distribution. Additionally, the lift force contribution from the wake-informed LL model is compared with the total blade loading from RANS to assess the feasibility of using the wake-informed LL model without external polar data.

2) For total blade loading comparison, using external polar data, the profile drag contributions are estimated and combined with the lift force contributions from the wake-informed LL model to calculate total thrust and power distributions. These results are then compared with RANS data for a practical evaluation of the performance of the wake-informed LL model.

First, the comparisons are presented for the attached flow condition, followed by the separated flow condition.

1. *Attached Flow Condition ($J = 0.60$)*

Figure 13 presents the comparison of thrust and power distributions for the attached flow condition. The mean solution obtained using the wake-informed LL is depicted with solid lines, and the 95% confidence interval is shown as a shaded area. The mean values and the confidence interval are based on 100 different sets of control points, which have been shown to provide converged results; see Fig. 8.

Figure 13a demonstrates excellent agreement between the wake-informed LL model and RANS results for the thrust distribution, both with and without the profile drag contribution. Without the profile drag contribution, the c_{t_L} values predicted using the wake-informed LL model slightly overpredict the peak value by 0.3% with a ±2.1% uncertainty compared to the total thrust distribution from RANS. Incorporating the profile drag component into the wake-informed LL model using polar data results in a 1.0% underprediction of the peak with a similar ±2.1% uncertainty. In contrast, the load-informed LL model suggests a 1.8% drag contribution by comparing its c_{t_L} distribution to the RANS c_t. These observations indicate potential underestimations in both the profile drag values from polar data and the lift values from the wake-informed LL model. Nonetheless, these results validate the wake-informed LL method for estimating thrust distributions from slipstream data, both with and without profile drag

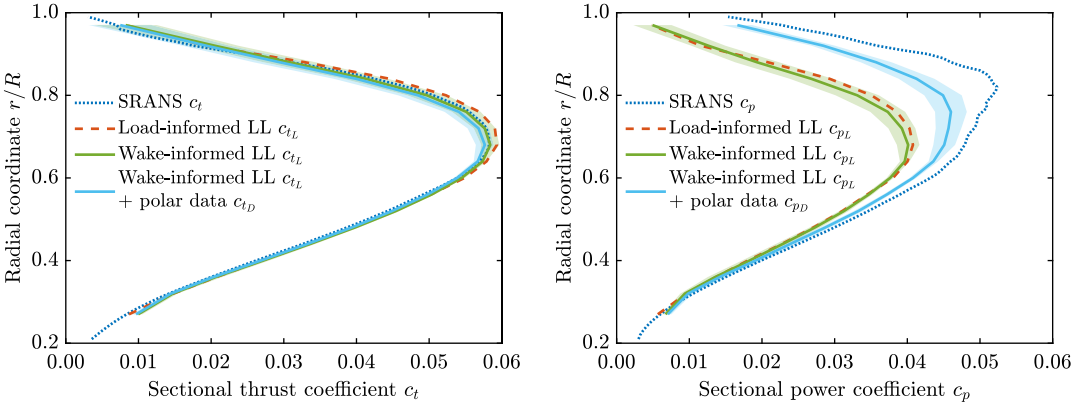

a) Sectional thrust coefficient b) Sectional power coefficient

Fig. 13 Comparison of blade loading distribution for the attached flow condition ($J = 0.60, T > 0$).

estimation. It should be noted that the profile drag estimation requires detailed propeller geometry information.

Figure 13b shows the comparison of power distributions. The comparison of the lift component of the power distribution c_{p_L} from the load-informed LL model and total power distribution c_p from RANS shows that the profile drag contribution c_{p_D} constitutes up to 10% of the c_p for $r/R \leq 0.50$, increasing to about 20% at $r/R = 0.75$, and even higher further outboard. Therefore, while the wake-informed LL model shows good agreement with the c_{p_L} obtained using the load-informed LL model, significant differences are observed when compared to c_p from RANS. When the profile drag contribution is included, the resulting power distributions from the wake-informed LL model become more representative. However, there is still an underprediction of up to 8% for $r/R \leq 0.75$, increasing to 13% at $r/R = 0.80$ and becoming even more pronounced farther outboard when compared to the total power distribution. This underprediction is attributed to the underestimation of profile drag values in the polar data as well as inaccuracies in the predicted induced angles of attack by LL models that result in an incorrect lift contribution to the power distribution.

Given the significance of the drag contribution, the wake-informed LL model should not be used for obtaining power distributions without accounting for the profile drag contribution via external polar data, which necessitates knowledge of the propeller geometry.

2. *Separated Flow Condition ($J = 1.10$)*

Figure 14 shows the comparison of blade loading distributions for the separated flow condition. The flow separation around blades [9,21] increases the importance of the drag contribution in the total thrust and power distributions. As per the load-informed LL model, profile drag accounts for 8.9% of the total thrust magnitude at $r/R = 0.76$, as shown by the comparison of c_t from RANS and c_{t_L} from the load-informed LL model in Fig. 14a.

The wake-informed LL model captures the radial gradients and overall shape of the thrust distribution seen in RANS but shows significant quantitative differences. These differences include a shift in the peak location from $r/R = 0.76$ in the RANS data to $r/R = 0.80$ and a 10.4% underprediction of the peak value with a $\pm 3.2\%$ uncertainty when not accounting for profile drag. Incorporating profile drag into the wake-informed LL model reduces the underprediction of the peak value to 3.9% with an associated uncertainty of $\pm 3.4\%$ as compared to RANS. These differences are attributed to the inviscid flow assumptions of the LL model, inaccuracies in the polar data, and the unaccounted influence of the presence of the spinner and nacelle (Appendix C). Although the slipstream data used in the wake-informed LL model implicitly incorporates some effects of the spinner and nacelle, the model does not explicitly account for their impact on blade loading.

Large differences are observed between the c_{t_L} values from load-informed and wake-informed LL models, with a 1.8% difference in the peak values and up to 20% difference near the root ($r/R \leq 0.40$), with load-informed LL as the reference. These larger discrepancies align with the significant differences observed in axial inductions in the slipstream in Fig. 12. These differences between load-informed LL and wake-informed LL are a consequence of pronounced viscous effects in the separated flow condition due to the flow separation around the blades [9], leading to different potential flow solutions obtained using direct blade loads and slipstream data.

Figure 14b shows the comparison of power distributions for the separated flow condition. When profile drag is not accounted for, the wake-informed LL model overpredicts the power distribution by more than 100% for $r/R \geq 0.65$ as compared to RANS. Incorporating profile drag estimates from polar data into the wake-informed LL model improves the radial trends, aligning it better with the power distribution from RANS. However, significant discrepancies are observed in absolute values, particularly in the outboard region, with a difference of 20% and higher for $r/R \geq 0.65$. Additionally, increased uncertainties of approximately 13% or more (with mean values as the reference) are observed for $r/R \geq 0.80$.

The increased uncertainty can be attributed to vortices being shed by the propeller blade in this outboard region due to flow separation. Consequently, the wake-informed LL model shows high sensitivity to the placement of control points, resulting in significant uncertainty in the converged bound circulation. The resultant uncertainty is reflected in the corresponding lift coefficient, which impacts the calculated drag coefficient from polar data and, subsequently, the power distribution.

C. Integrated Thrust and Power

This section compares the integrated thrust and power values from the wake-informed LL method with those obtained from RANS simulations. In practical applications, the contributions of the blade and spinner are typically inseparable. However, the wake-informed LL model does not account for the influence of the spinner. Therefore, to provide an estimate of the expected difference caused by the presence of the spinner, the wake-informed LL model is compared to both blade-only and blade plus spinner results from RANS simulations.

Table 2 lists the integrated thrust and power coefficient values for the attached flow condition. The comparison of the integrated values with and without the spinner shows that the spinner accounts for 1.3 and 0.7% of the total integrated thrust and power, respectively. When the profile drag is not included, the wake-informed LL model slightly overpredicts the integrated thrust by 0.4% with an uncertainty of 1.3% relative to the total integrated thrust from RANS. This corresponds to a 1.7% overprediction compared to the blade-only contribution in RANS simulations. Conversely, incorporating the profile drag contribution via external polar data results in a 1.6% underprediction of integrated thrust compared to the total value, with a negligible underprediction (0.3%) relative to the RANS blade-only contribution.

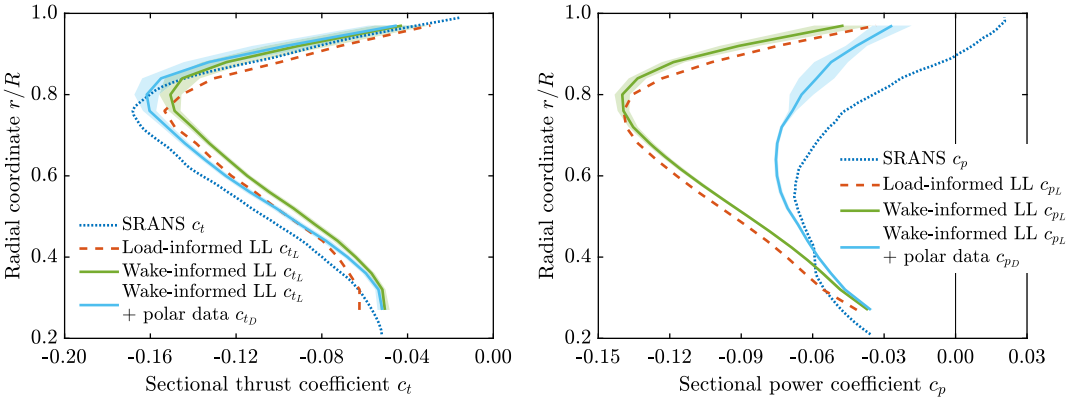

a) Sectional thrust coefficient **b) Sectional power coefficient**

Fig. 14 Comparison of blade loading distribution for the separated flow condition ($J = 1.10, T < 0$).

Table 2 Comparison of integrated thrust and power between RANS and the wake-informed lifting line model for the attached flow condition ($J = 0.60, T > 0$)

Method	Components	C_T	$\Delta C_T\%$	C_P	$\Delta C_P\%$
RANS	Blades plus spinner	+0.0410		0.0385	
RANS	Blades	+0.0405	−1.3	0.0382	−0.7
Wake-informed LL	Blades	+0.0411 ± 0.0005	+0.4 ± 1.3	0.0277 ± 0.0004	−28.1 ± 1.0
Wake-informed LL plus polar data	Blades	+0.0403 ± 0.0005	−1.6 ± 1.3	0.0343 ± 0.0003	−11.0 ± 0.8

For power, the wake-informed LL model exhibits significant errors compared to RANS. Without accounting for the profile drag contribution, the wake-informed LL model underpredicts the power by 28.1% as compared to the total integrated power from RANS. Incorporating the profile drag contribution via external polar data reduces this underprediction to 11.0%.

Therefore, while the wake-informed LL model shows strong agreement with RANS for thrust predictions, even without accounting for profile drag, significant errors are observed in the integrated power values even after including the profile drag contribution. These findings are consistent with previous comparisons of the radial thrust and power distribution shown in Figs. 13a and 13b.

Table 3 lists the integrated thrust and power values for the separated flow condition. In this case, the spinner accounts for 1.9% of the total thrust magnitude. The wake-informed LL model underpredicts thrust magnitude by 13.1% with an uncertainty of 2.0% as compared to the total integrated thrust magnitude obtained from RANS. Including the profile drag contribution using external polar data reduces this underprediction to 6.8% with an uncertainty of 2.1%. This improvement highlights the increased significance of profile drag in the separated flow condition due to flow separation. These error magnitudes align with the discrepancies observed in the thrust distributions shown in Fig. 14a.

For the power, the spinner has a significant contribution of 6.6% to the total power, as also detailed in Appendix C. When not accounting for the profile drag contribution, the wake-informed LL model overpredicts the power magnitude by 92.6% due to the increased importance of the profile drag contribution due to the flow separation. Incorporating profile drag using polar data reduces this overprediction to 21.1%. These discrepancies are a result of delayed stall prediction in the polar data, leading to underestimated profile drag and an overpredicted power. Additionally, errors in the induced angle of attack also affect the lift contribution to power.

VI. Experimental Test Case

This section applies the wake-informed LL model to experimental PIV data from Nederlof et al. [10] to demonstrate its capabilities and potential for expanding experimental analyses. The model was applied to the same operating conditions ($J = 0.60, 1.10$) for which the model was validated in the previous section using RANS data. Figure 15 shows the phase-locked out-of-plane vorticity field obtained from PIV measurements for both operating conditions, along with the identified shape of the blade wake intersecting the measurement plane, represented by solid black lines. A fifth-order polynomial was used to define the blade wake shapes for the attached flow condition, while a sixth-order polynomial was used for the separated flow condition (obtained using the procedure defined in Sec. IV.B).

The analysis begins by comparing input axial inductions from PIV with output axial inductions from the wake-informed LL model. Subsequently, measured thrust is compared with thrust obtained from the wake-informed LL model. Finally, thrust distributions, local angles of attack, and sectional lift coefficients derived from the wake-informed LL model are presented.

A. Axial Induction

Figure 16 shows the comparison of axial inductions from PIV data and wake-informed LL model for the attached flow condition. Similar to the validation case, the most significant errors are observed close to the blade due to the inability of the LL models to simulate the thickness effect of the propeller blades; see

Table 3 Comparison of integrated thrust between RANS and the wake-informed lifting line model for the separated flow condition ($J = 1.10, T < 0$)

Method	Components	C_T	$\Delta C_T\%$	C_P	$\Delta C_P\%$
RANS	Blades plus spinner	−0.1272		−0.0548	
RANS	Blades	−0.1248	−1.9	−0.0512	−6.6
Wake-informed LL	Blades	−0.1106 ± 0.0025	−13.1 ± 2.0	−0.1056 ± 0.0021	92.6 ± 3.8
Wake-informed LL plus polar data	Blades	−0.1186 ± 0.0027	−6.8 ± 2.1	−0.0663 ± 0.0011	21.1 ± 2.0

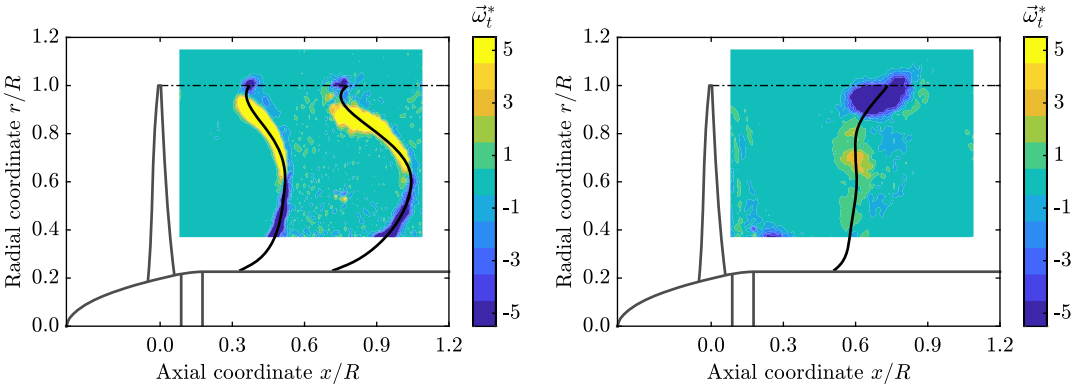

a) Attached flow condition ($J = 0.60, T > 0$) **b) Separated flow condition ($J = 1.10, T < 0$)**

Fig. 15 Phase-locked nondimensional out-of-plane vorticity component ω_t^* obtained from PIV measurement along with the identified shape of blade wakes and tip vortices.

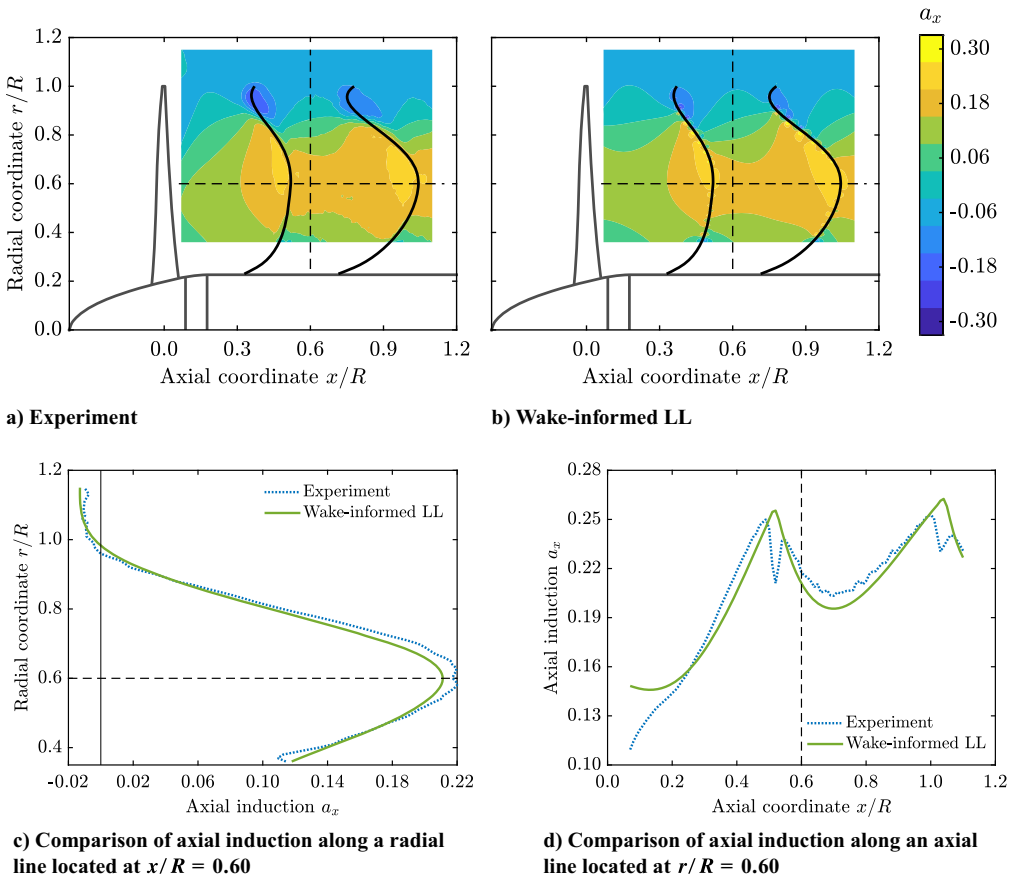

Fig. 16 Comparison of axial induction in the slipstream for the attached flow condition ($J = 0.60, T > 0$).

Figs. 16a and 16b. Away from the propeller blades ($x/R \geq 0.20$), there is a good agreement between the experimental inductions and those obtained from the wake-informed LL model. This agreement is further confirmed in the radial and axial line plots at $x/R = 0.60$ and $r/R = 0.60$, respectively, as seen in Figs. 16c and 16d. The line plot at $x/R = 0.60$ shows good agreement except for an underprediction of the peak value by 2.9% (Fig. 16c).

Similarly, good agreement is also observed along the axial line at $r/R = 0.60$ in Fig. 16d, except for $x/R \leq 0.20$. Notably, the peak values near blade wakes are sharper in LL models due to their inviscid flow assumption, contrasting with the more flattened peaks in experiments (due to viscous effects). Additionally, some noise can be observed in the experimental data in the line plot, particularly between $0.6 \leq x/R \leq 1.0$, which is not simulated by the wake-informed LL model. Given the minimal differences between the experimental and wake-informed LL axial inductions, it is expected that the thrust distributions obtained from the latter method should closely represent the experimental blade loading for the considered operating condition.

Figure 17 shows the comparison of axial induction in the slipstream for the separated flow condition. As expected, significant discrepancies are observed close to the propeller for $x/R \leq 0.30$ (due to the blade thickness effect). Away from the blade, a qualitative agreement is observed between the experimental and wake-informed LL axial inductions. However, some differences are evident in the contour plots near the tip vortex region. The vorticity shed by the blades due to the flow separation in this operating condition is not accurately modeled by the wake-informed LL model due to the inviscid assumption.

To further analyze these discrepancies, two line plots are presented: a radial line at $x/R = 0.90$ and an axial line at $r/R = 0.60$. The comparison along the radial line ($x/R = 0.90$) shows that the wake-informed LL model captures the radial gradients, although there are differences in absolute values. The differences are negligible for $r/R \leq 0.60$ but increase to 10% in the outboard region ($r/R = 0.80$). The axial line plot at $r/R = 0.60$ shows significant discrepancies between the experiment and wake-informed LL model, particularly for $x/R \leq 0.30$ due to the thickness effect of the propeller blade. Beyond this region, the trends are captured, but with notable differences in the gradients. The wake-informed LL model exhibits a steeper gradient for axial induction increase for $x/R \leq 0.60$ and a lower gradient for $x/R \geq 0.80$ compared to the experiment. These differences in the gradient are expected to be a consequence of assumptions made about wake geometry and convection velocity within the LL model. Besides, as the axial line passes the location where the blade wake intersects through the plane (near $x/R = 0.60$), a local peak is seen in the wake-informed LL model, whereas a sudden drop in the axial induction values is seen in the experimental data. This discrepancy is attributed to the inviscid flow assumption of the LL model, while the experimental data capture the viscous nature of the blade wake, which is not concentrated around the assumed vortex line.

Given the significant differences between the axial inductions obtained from the experiment and the wake-informed LL model, it can be concluded that the thrust distributions obtained from the wake-informed LL model for this separated flow condition are expected to have significant errors in terms of absolute values. However, the model might still be able to capture the radial gradients of the experimental thrust distribution, as evident from the comparison of the axial inductions along the radial line at $x/R = 0.90$.

B. Integrated Thrust and Power

In cases where the measured integrated thrust and power values are available, comparing them to wake-informed LL model predictions provides an additional means to estimate the potential error in the predicted thrust and power distribution. This section compares the integrated thrust obtained using the wake-informed LL model with those measured in the experiments. The experimental values reported here were corrected for wind-tunnel boundary interference. Details of these corrections can be found in previous work by the authors [9].

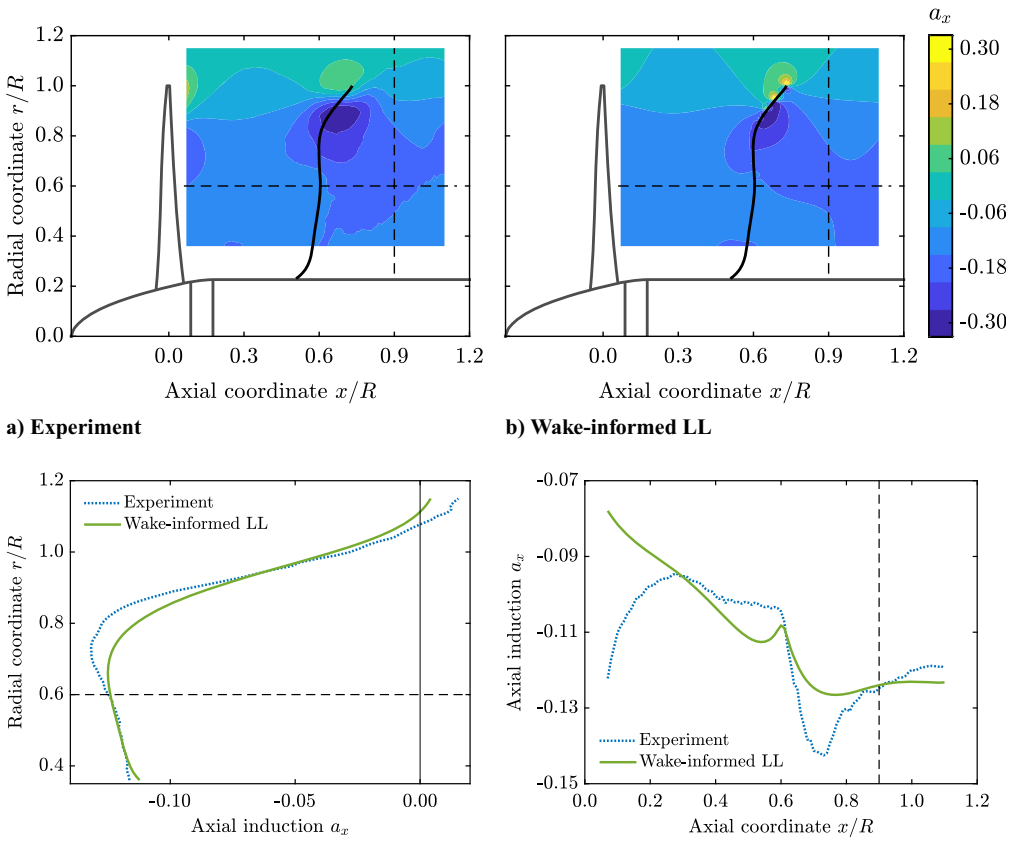

Fig. 17 Comparison of axial induction in the slipstream for the separated flow condition ($J = 1.10, T < 0$).

Table 4 lists the integrated thrust and power values from the experiment and the wake-informed LL model for the attached flow condition. The experimental thrust and power have uncertainties of 2.4 and 1.3%, respectively. The wake-informed LL model underpredicts thrust by 2.2% (with a 2.6% uncertainty) and power by 31.5% (with a 1.5% uncertainty) compared to experimental values. Incorporating drag contributions using polar data increases the thrust underprediction to 4.2% due to negative drag contributions in the thrust direction while reducing the power underprediction to 14.2% due to significant positive drag contributions in the torque direction. A part of these discrepancies can be attributed to the presence of the spinner and nacelle in the experiments, which are not modeled in the wake-informed LL model. The error in the thrust is of the same order as observed in the validation case for the same operating condition. The underprediction of integrated thrust, with and without polar data, being comparable to the uncertainty in experimental measurements, suggests that the wake-informed LL model can provide reasonable thrust distribution predictions for this attached flow condition. However, the power distributions obtained from the wake-informed LL model should be interpreted with caution while ensuring that profile drag contributions are accurately accounted for.

Table 5 lists the integrated thrust and power values for the separated flow condition. Unlike the attached flow case, the uncertainties in the experimental values are rather small ($\pm 0.5\% - \pm 0.6\%$). For this condition, the wake-informed LL model without polar data underpredicts thrust by 12.7% (with a 2.5% uncertainty) and overpredicts power by 95.4% (with a 4.6% uncertainty) for this condition. These larger errors in the integrated values for the separated flow case, compared to the attached flow case, are consistent with previously

Table 4 Comparison of integrated thrust and power between the experiment and wake-informed lifting line model for the attached flow condition ($J = 0.60, T > 0$)

Method	Components	C_T	$\Delta C_T\%$	C_P	$\Delta C_P\%$
Experiment	Blades plus spinner	$+0.0423 \pm 0.0010$	± 2.4	$+0.0416 \pm 0.0006$	± 1.3
Wake-informed LL	Blades	$+0.0414 \pm 0.0003$	-2.2 ± 2.6	$+0.0285 \pm 0.0003$	-31.5 ± 1.5
Wake-informed LL with polar data	Blades	$+0.0406 \pm 0.0003$	-4.2 ± 2.6	$+0.0357 \pm 0.0003$	-14.2 ± 1.5

Table 5 Comparison of integrated thrust and power between the experiment and the wake-informed lifting line model for the separated flow condition ($J = 1.10, T < 0$)

Method	Components	C_T	$\Delta C_T\%$	C_P	$\Delta C_P\%$
Experiment	Blades plus spinner	-0.1298 ± 0.0007	± 0.5	-0.0553 ± 0.0003	± 0.6
Wake-informed LL	Blades	-0.1133 ± 0.0031	-12.7 ± 2.5	-0.1081 ± 0.0025	$+95.4 \pm 4.6$
Wake-informed LL with polar data	Blades	-0.1216 ± 0.0034	-6.3 ± 2.7	-0.0659 ± 0.0016	$+19.1 \pm 2.9$

observed increased discrepancies in axial induction between experiments and the wake-informed LL model for the former (Fig. 17). The increased drag contribution in this operating condition, caused by flow separation, combined with the inherent limitations of the LL model, exacerbates these errors. Incorporating drag contributions reduces the thrust underprediction to 6.3% and the power overprediction to 19.1%. These results highlight the necessity of accounting for drag contributions using external polar data when predicting thrust and power distributions with the wake-informed LL model in separated flow conditions.

C. Blade Loading Distributions

This section gives an example of the blade loading parameters that can be derived from the slipstream velocity field of an experimental test case. In addition to thrust and power distributions, the sectional lift coefficient, drag coefficient, and local angles of attack at the blade sections are also presented in Fig. 18.

Figure 18a shows the radial distributions of the sectional thrust coefficient obtained using the wake-informed LL model, both with and without estimated drag contributions using the polar data. For the attached flow condition ($J = 0.60$), the peak loading is observed around $r/R \approx 0.7$, while for the separated flow condition ($J = 1.10$), it shifts to $r/R \approx 0.85$ as per the wake-informed LL model. The attached flow condition exhibits negative loading at the tip, consistent with previous studies for this propeller and operating condition [10]. The attached flow case has a relatively small uncertainty of $\pm 1.0\%$, whereas the separated flow case shows an uncertainty of $\pm 4.2\%$ at the peak. Incorporating drag contributions has a minimal impact on the thrust distribution for the attached flow condition, with changes of around 1 and 2% along the entire blade span. In contrast, for the separated flow condition, drag contributions significantly influence the thrust distribution due to the increased importance of drag as a result of the flow separation, resulting in up to 9% changes along the blade span when compared to the distribution without drag contributions.

Figure 18b shows the power distributions along the blade span obtained using the wake-informed LL model with and without estimated drag contributions. For the attached flow case, the power values predicted without the drag contribution exhibit similar trends and magnitudes as those including drag for $r/R \leq 0.50$. However, drag contributions become increasingly significant outboard, accounting for 10% at $r/R = 0.70$ and 33% at $r/R = 0.80$, compared to the power distribution without drag contributions as the reference. In the separated flow condition, the drag contribution dramatically alters the power distribution along the entire span, reducing power by 10% at $r/R = 0.40$, increasing to a 70% reduction at $r/R = 0.90$ when compared to the distribution without drag contributions.

Notably, power distributions with drag contributions exhibit significant uncertainty (up to 38%) for $r/R \geq 0.80$ in the separated flow condition. This uncertainty arises due to the shedding of vortices in the outboard region caused by flow separation. Consequently, the wake-informed LL model shows increased sensitivity to the placement of control points in this region, resulting in increased uncertainty in the converged bound circulation. The resulting uncertainty is reflected in the corresponding lift coefficient (Fig. 18c), which impacts the calculated drag coefficient from polar data and, subsequently, the power distribution.

The distribution of the sectional lift coefficient along the blade span obtained from the wake-informed LL model is shown in Fig. 18c. In the attached flow case, the lift coefficient reaches a maximum of 0.5 near $r/R = 0.5$, then decreases with the increasing radial coordinate and goes below zero for $r/R > 0.9$. In contrast, the sectional lift coefficient in the separated flow condition decreases from -1.0 to -0.5 up to the radial coordinate of 0.90 and then quickly drops towards zero at the tip.

Figure 18d shows the distribution of the drag coefficient along the blade span, obtained by interpolating the polar data at the c_l values obtained using the wake-informed LL model. The drag values for the separated flow condition are nearly an order of magnitude higher than those for the attached flow condition, therefore justifying the previously observed increased importance of the drag contribution in the thrust and power distributions. In the outboard region ($r/R > 0.80$), the drag coefficient exhibits significant uncertainty (up to 28%) for the separated flow condition. This is attributed to the higher uncertainty in the converged bound circulation (as explained before), which was also reflected in the power distribution in Fig. 18b.

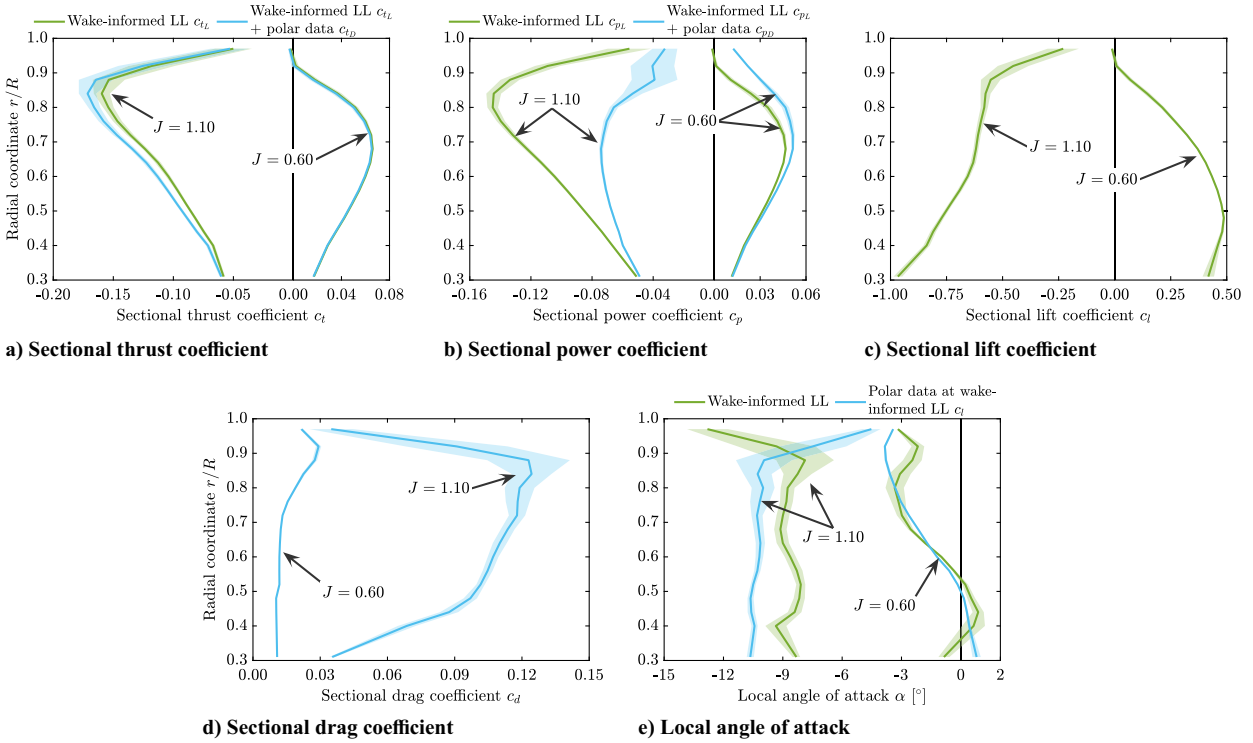

a) Sectional thrust coefficient **b) Sectional power coefficient** **c) Sectional lift coefficient**

d) Sectional drag coefficient **e) Local angle of attack**

Fig. 18 Comparison of blade loading distributions for the attached and separated flow conditions obtained using the wake-informed lifting line model with PIV data as input.

Figure 18e shows the distribution of the local angle of attack at blade sections. As per the wake-informed LL model, the positively cambered airfoils of the propeller blade operate at a significantly higher absolute angle of attack in the separated flow conditions compared to the attached flow condition. While the separated flow condition maintains relatively constant local angles of attack (between $-10°$ and $-8°$) up to $r/R \leq 0.9$, the attached flow condition exhibits a broader range of $-4°$–$1°$. The angles of attack obtained from the polar data for the given c_l based on the wake-informed LL model are also plotted in the figure. For the attached flow condition, polar data predictions align well with wake-informed LL model trends, with differences of less than 0.5° (except at the root and the tip). However, for the separated flow condition, the use of the polar data overpredicts the required angles of attack to obtain the given c_l by 1.1°–2.5° along the whole blade span (except at the tip). This mismatch could either be the consequence of the inaccuracies in the polar data and/or due to the assumptions of the LL model being challenged under these conditions, potentially leading to an incorrect induced angle of attack at the blade.

VII. Conclusions

This paper evaluated the performance of the so-called *wake-informed lifting line* model in estimating blade loading distributions from slipstream velocity data. The method was validated by comparing its results with those obtained from RANS simulations and subsequently applied to a test case based on experimental input data. Because the wake-informed LL model only predicts the lift component of the blade loading distribution, drag contributions were incorporated using external polar data.

In the attached flow condition, the wake-informed LL model demonstrated excellent agreement with RANS predictions for thrust distribution, with errors below 1% in the peak value, even without accounting for the drag contribution. In the separated flow condition, while the model qualitatively captured the radial trends and overall thrust distribution shape, discrepancies of 10–20% were observed in absolute values when drag contributions were not included. Accounting for drag reduced these errors to 8–16%, with the remaining discrepancies attributed to the limitations of potential flow models in separated flows, inaccuracies in external polar data, and unaccounted influence of the spinner.

Irrespective of the flow condition (attached or separated), the drag contribution is crucial in the torque direction and must be accounted for when estimating the power distribution using the wake-informed LL model, necessitating the use of external polar data. Even with the drag contribution included, power values were underestimated by 10–25% in the outboard region ($r/R \geq 0.80$) in the attached flow condition and more than 20% for the separated flow condition beyond $r/R \geq 0.65$. This underprediction is attributed to two factors: the underestimation of drag in the polar data and inaccuracies in the induced angles of attack predicted by the wake-informed LL model, leading to an inaccurate lift contribution to the power distribution.

When applied to experimental data, the model provided the thrust distribution, sectional lift coefficients, and local angles of attack post priori from slipstream velocity measurements, without the need for propeller geometry or external polar data (assuming drag contributions are negligible). The resulting axial induction and integrated thrust obtained using this method showed errors of approximately 2 and 3% for the attached flow condition and more than 10% for the separated flow condition.

In conclusion, the wake-informed LL model offers a promising, nonintrusive approach for estimating blade loading distributions and local flow conditions at the blade, post priori from slipstream velocity measurements. It offers significant value for practical applications, particularly in predicting thrust distributions when propeller geometry is unknown or inaccessible, as well as in situations where blade instrumentation is not feasible. However, for the estimation of power distribution, external polar data are required, which inherently requires the knowledge of propeller geometry. Although the model excels in attached flow conditions, its limitations in separated flow necessitate caution in its application under such conditions. Future research should focus on extending the model's applicability to more complex operating conditions, including rotors at nonzero incidence angles and operations in unsteady or turbulent flow environments.

Appendix A: RANS Simulation Setup

The RANS equations for compressible flow were solved using ANSYS® Fluent 2019 R3 [22], which is a commercial, unstructured, finite-volume, cell-centered solver. As only uniform inflow conditions have been studied in this paper, these simulations were solved for a single-blade wedge domain in a steady manner using a multireference-frame approach. The computational domain used for these simulations can be seen in Fig. 19. It was ensured that the boundaries of the domains were sufficiently far away to keep the influence of boundary conditions on the flow properties near the propeller blade minimum, following typical values for domain sizes for isolated propeller simulations used in earlier work [23–25]. The height of the block of the domain in the vicinity of the propeller blade was chosen to be $1.5R$ to allow for wake expansion in negative thrust conditions and was refined to capture the strong gradients in flow properties in the propeller slipstream. The height of the domain was chosen to be $1.0R$ with a wedge angle of 120°.

Following the CFD setup of previous research efforts for similar problems [23–25], total-pressure inlet, pressure outlet, and pressure far-field boundary conditions were used in combination with a conformal periodic boundary condition for the side boundaries to avoid interpolation errors. The propeller blade and spinner were modeled as no-slip stationary walls in the moving reference frame, and the nacelle was modeled as a no-slip stationary wall in the absolute reference frame. The air density was calculated using the ideal gas assumption, and the dynamic viscosity was computed using Sutherland's law. The turbulence modeling was based on the Spalart–Allmaras method with a modification proposed by Dacles-Mariani et al. [26,27] The details of the grid convergence study of the setup can be found in the authors' previous work [9].

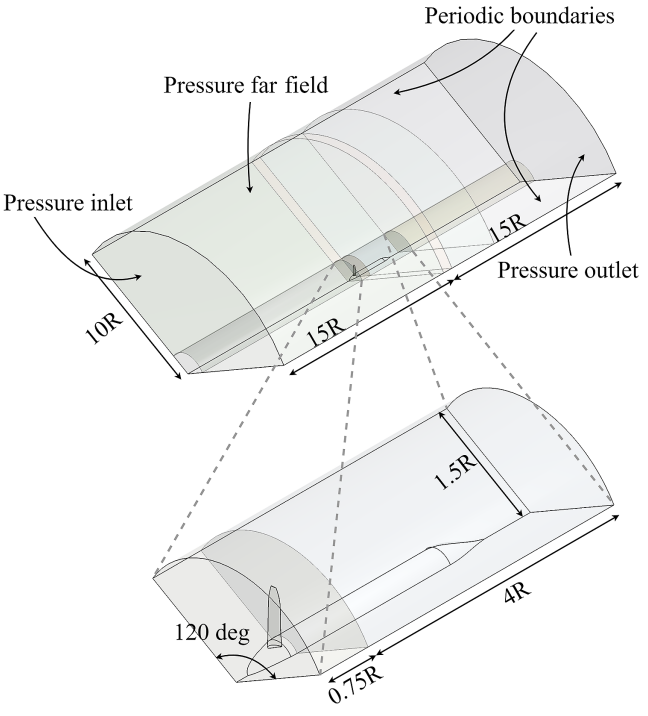

Fig. 19 Numerical domain and boundary conditions for steady RANS simulations.

Appendix B: Adaptation of the Blade Wake Identification Process in Absence of Vorticity Field

In cases where only the axial velocity component is available, ω_t^* values cannot be computed, necessitating an alternative approach to determine the location and shape of the blade wake. A viable method is to analyze the gradient of the axial velocity in the axial direction ($\partial V_x/\partial x$). Because the blade wake is a viscous region characterized by a locally reduced axial velocity, this gradient is expected to be negative within the wake.

This approach is demonstrated in Fig. 20, in which the non-dimensionalized gradient of the axial velocity, $(\partial V_x/\partial x)(D/V_\infty)$, is plotted alongside the previously detected blade wake and tip vortex shapes derived from ω_t^* values using the process described in Sec. IV.B (indicated by solid black lines). The strong alignment of the previously identified blade wake and tip vortex with regions of negative $(\partial V_x/\partial x)(D/V_\infty)$ values validates the proposed approach.

Appendix C: Influence of Spinner and Nacelle on Blade Loading

Generally, LL models do not account for the presence of the spinner and nacelle. This Appendix assesses the impact of these components on blade loading distributions by comparing RANS simulations with and without the spinner and nacelle. Figure 21 presents the thrust and power distributions along the blade span for both the attached flow condition ($J = 0.60$) and the separated flow condition ($J = 1.10$), with and without the presence of the spinner and nacelle. For the attached flow condition, the presence of the spinner and nacelle has a negligible effect on the thrust and power

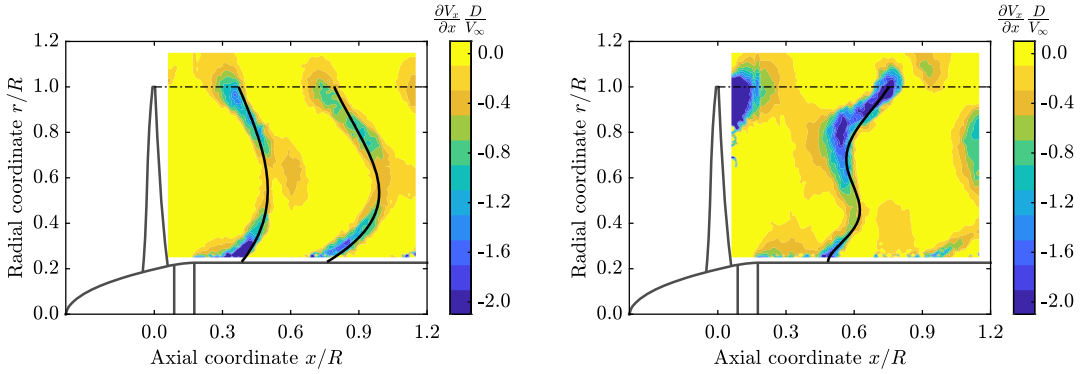

a) Attached flow condition ($J = 0.60, T > 0$) **b) Separated flow condition ($J = 1.10, T < 0$)**

Fig. 20 Phase-locked non-dimensional gradient of the axial velocity in the axial direction $(\partial V_x/\partial x)(D/V_\infty)$ obtained from RANS simulations.

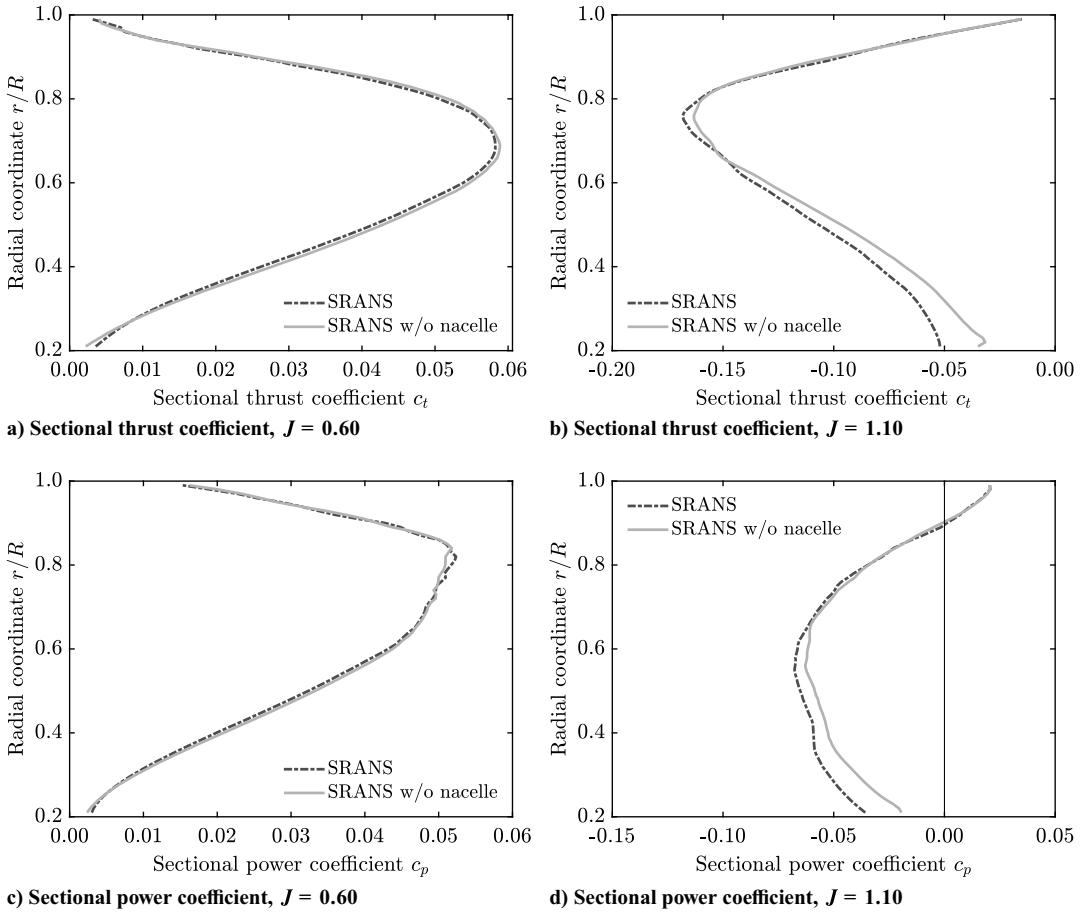

a) Sectional thrust coefficient, $J = 0.60$ **b) Sectional thrust coefficient, $J = 1.10$**

c) Sectional power coefficient, $J = 0.60$ **d) Sectional power coefficient, $J = 1.10$**

Fig. 21 Effect of the presence of spinner and nacelle on the blade loading for the attached ($J = 0.60$) and the separated flow conditions ($J = 1.10$).

distributions (Figs. 21a and 21c), with differences around 1% near the peak value for thrust and 3% for power, using the RANS results with nacelle and spinner as the reference.

In contrast, the spinner and nacelle significantly affect the blade loading distribution in the separated flow condition (Figs. 21b and 21d), particularly for radial positions up to $r/R \approx 0.80$. The RANS simulations without the spinner and nacelle underpredict the thrust coefficient by more than 15% for $r/R \leq 0.40$ and between 0 and 15% for $0.40 \leq r/R \leq 0.65$, along with the underprediction of the peak value by 3%, as compared to the RANS simulation with the spinner and nacelle. Similar trends are observed for the power distribution, with an error of more than 11% for $r/R \leq 0.40$ and between 2 and 11% for $0.40 \leq r/R \leq 0.65$. This comparison reveals that the error from neglecting the spinner and nacelle is more significant under the separated flow condition than the attached flow condition. Incorporating the effects of the spinner and nacelle into LL models could be partially achieved through the use of panel methods.

Acknowledgments

The research leading to these results is part of the FUTPRINT50 project. This project has received funding from the European Union's Horizon 2020 Research and Innovation programme under grant agreement number 875551. The authors would like to thank Robert Nederlof for providing the experimental data for the validation of the method.

Code Availability

The example source code for the wake-informed lifting line model, implemented in MATLAB® for this study, is available in the 4TU.ResearchData repository [1]. Please note that the code is provided as an example for the specific data set used in this study and may not be directly compatible with other data sets. Additionally, it has not been optimized for performance.

References

[1] Goyal, J., "Wake-Informed Lifting Line Theory: Example Code, *4TU.ResearchData.Software*, 2024. https://doi.org/10.4121/4bf0f63f-7ac2-48dc-a2b1-e3fb819b34c2

[2] Philipsen, I., Hoeijmakers, H., and Hegen, S., "An Overview of Advanced Propeller Simulation Tests in the German Dutch Wind Tunnels (DNW)," *22nd AIAA Aerodynamic Measurement Technology and Ground Testing Conference*, AIAA Paper 2002-2920, June 2002. https://doi.org/10.2514/6.2002-2920

[3] Sinnige, T., Ragni, D., Eitelberg, G., and Veldhuis, L. L. M., "Pusher-Propeller Blade Loading with and Without Pylon Trailing-Edge Blowing," *34th AIAA Applied Aerodynamics Conference*, AIAA Paper 2016-3421, June 2016. https://doi.org/10.2514/6.2016-3421

[4] Brown, F., Fleming, J., Langford, M., Walton, W., Ng, W., Schwartz, K., Wisda, D., and Burdisso, R., "Reduced-Order Prediction of Unsteady Propeller Loading and Noise from Pylon Wake Ingestion," *AIAA Journal*, Vol. 59, No. 9, 2021, pp. 3304–3316. https://doi.org/10.2514/1.J060109

[5] Ragni, D., van Oudheusden, B. W., and Scarano, F., "Non-Intrusive Aerodynamic Loads Analysis of an Aircraft Propeller Blade," *Experiments in Fluids*, Vol. 51, No. 2, 2011, pp. 361–371. https://doi.org/10.1007/s00348-011-1057-7

[6] del Campo, V., Ragni, D., Micallef, D., Akay, B., Diez, F. J., and Simão Ferreira, C., "3D Load Estimation on a Horizontal Axis Wind Turbine Using SPIV," *Wind Energy*, Vol. 17, No. 11, 2014, pp. 1645–1657. https://doi.org/10.1002/we.1658

[7] del Campo, V., Ragni, D., Micallef, D., Akay, B., Diez, F. J., and Simão Ferreira, C. J., "Estimation of Loads on a Horizontal Axis Wind Turbine Operating in Yawed Flow Conditions," *Wind Energy*, Vol. 18, No. 11, 2015, pp. 1875–1891. https://doi.org/10.1002/we.1794

[8] Haans, W., van Kuik, G., and van Bussel, G., "The Inverse Vortex Wake Model: A Measurement Analysis Tool," *45th AIAA Aerospace Sciences Meeting and Exhibit*, AIAA Paper 2007-422, Jan. 2007. https://doi.org/10.2514/6.2007-422

[9] Goyal, J., Sinnige, T., Avallone, F., and Ferreira, C., "Benchmarking of Aerodynamic Models for Isolated Propellers Operating at Positive and Negative Thrust," *AIAA Journal*, Vol. 62, No. 10, 2024, pp. 3758–3775. https://doi.org/10.2514/1.J064093

[10] Nederlof, R., Ragni, D., and Sinnige, T., "Energy-Harvesting Performance of an Aircraft Propeller," *Journal of Aircraft*, Vol. 62, No. 2, 2025, pp. 349–369. https://doi.org/10.2514/1.C038005

[11] Katz, J., and Plotkin, A., *Low-Speed Aerodynamics*. Vol. 13, Cambridge Univ. Press, New York, 2001, pp. 331–340. https://doi.org/10.1017/CBO9780511810329

[12] Byrd, R. H., Gilbert, J. C., and Nocedal, J., "A Trust Region Method Based on Interior Point Techniques for Nonlinear Programming," *Mathematical Programming*, Vol. 89, No. 1, 2000, pp. 149–185. https://doi.org/10.1007/PL00011391

[13] Coleman, T. F., and Li, Y., "An Interior Trust Region Approach for Nonlinear Minimization Subject to Bounds," *SIAM Journal on Optimization*, Vol. 6, No. 2, 1996, pp. 418–445. https://doi.org/10.1137/0806023

[14] DeLoach, R., "Improved Quality in Aerospace Testing Through the Modern Design of Experiments," *38th Aerospace Sciences Meeting and Exhibit*, AIAA Paper 2000-825, 2000. https://doi.org/10.2514/6.2000-825

[15] Veldhuis, L. L. M., *Propeller Wing Aerodynamic Interference*, Delft Univ. of Technology, Delft, The Netherlands, 2005, http://resolver.tudelft.nl/uuid:8ffbde9c-b483-40de-90e0-97095202fbe3.

[16] van Rooij, R., "Modification of the Boundary Layer Calculation in RFOIL for Improved Airfoil Stall Prediction," Report IW-96087R, Delft Univ. of Technology, Delft, The Netherlands, Sept. 1996.

[17] Drela, M., "XFOIL: An Analysis and Design System for Low Reynolds Number Airfoils," *Low Reynolds Number Aerodynamics*, edited by T. J. Mueller, Springer, Berlin, 1989, pp. 1–12.

[18] Yu, W., Zhang, M. M., and Xu, J. Z., "Effect of Smart Rotor Control Using a Deformable Trailing Edge Flap on Load Reduction under Normal and Extreme Turbulence," *Energies*, Vol. 5, No. 9, 2012, pp. 3608–3626. https://doi.org/10.3390/en5093608

[19] Snel, H., Houwink, R., and Bosschers, J., "Sectional Prediction of Lift Coefficients on Rotating Wind Turbine Blades in Stall," Report ECN-93-052, Energy Research Center of the Netherlands, Petten, The Netherlands, 1993.

[20] Bosschers, J., Montgomerie, B., Brand, A., and van Rooij, R., "Influence of Blade Rotation on the Sectional Aerodynamics of Rotational Blades," *22nd European Rotorcraft Forum*, England, 1996.

[21] Goyal, J., Avallone, F., and Sinnige, T., "Isolated Propeller Aeroacoustics at Positive and Negative Thrust," *Aerospace Science and Technology*, Vol. 147, 2024, Paper 109021. https://doi.org/10.1016/j.ast.2024.109021

[22] Anon, *ANSYS® Academic Research Release 2019 R3 Help System, Fluent*, ANSYS, Inc., Canonsburg, PA, 2019.

[23] Sinnige, T., Stokkermans, T. C. A., van Arnhem, N., and Veldhuis, L. L. M., "Aerodynamic Performance of a Wingtip-Mounted Tractor Propeller Configuration in Windmilling and Energy-Harvesting Conditions," *AIAA Aviation 2019 Forum*, AIAA Paper 2019-3033, June 2019. https://doi.org/10.2514/6.2019-3033

[24] Stokkermans, T. C. A., van Arnhem, N., Sinnige, T., and Veldhuis, L. L. M., "Validation and Comparison of RANS Propeller Modeling Methods for Tip-Mounted Applications," *AIAA Journal*, Vol. 57, No. 2, 2019, pp. 566–580. https://doi.org/10.2514/1.J057398

[25] van Arnhem, N., Vos, R., and Veldhuis, L. L. M., "Aerodynamic Loads on an Aft-Mounted Propeller Induced by the Wing Wake," *AIAA Scitech 2019 Forum*, AIAA Paper 2019-1093, Jan. 2019. https://doi.org/10.2514/6.2019-1093

[26] Spalart, P. R., and Allmaras, S. R., "A One-Equation Turbulence Model for Aerodynamic Flows," *30th Aerospace Sciences Meeting*, AIAA Paper 1992-439, June 1992. https://doi.org/10.2514/6.1992-439

[27] Dacles-Mariani, J., Zilliac, G. G., Chow, J. S., and Bradshaw, P., "Numerical/Experimental Study of a Wingtip Vortex in the Near Field," *AIAA Journal*, Vol. 33, No. 9, 1995, pp. 1561–1568. https://doi.org/10.2514/3.12826

F. Coton
Associate Editor